University of South-Eastern Norway
Faculty of Technology, Natural Sciences and Maritime Studies
—
Doctoral dissertation no. 88
2021

Uyen Phuong Do

Glucose energy harvester for self-powering of remote distributed bioanalytical microsystems

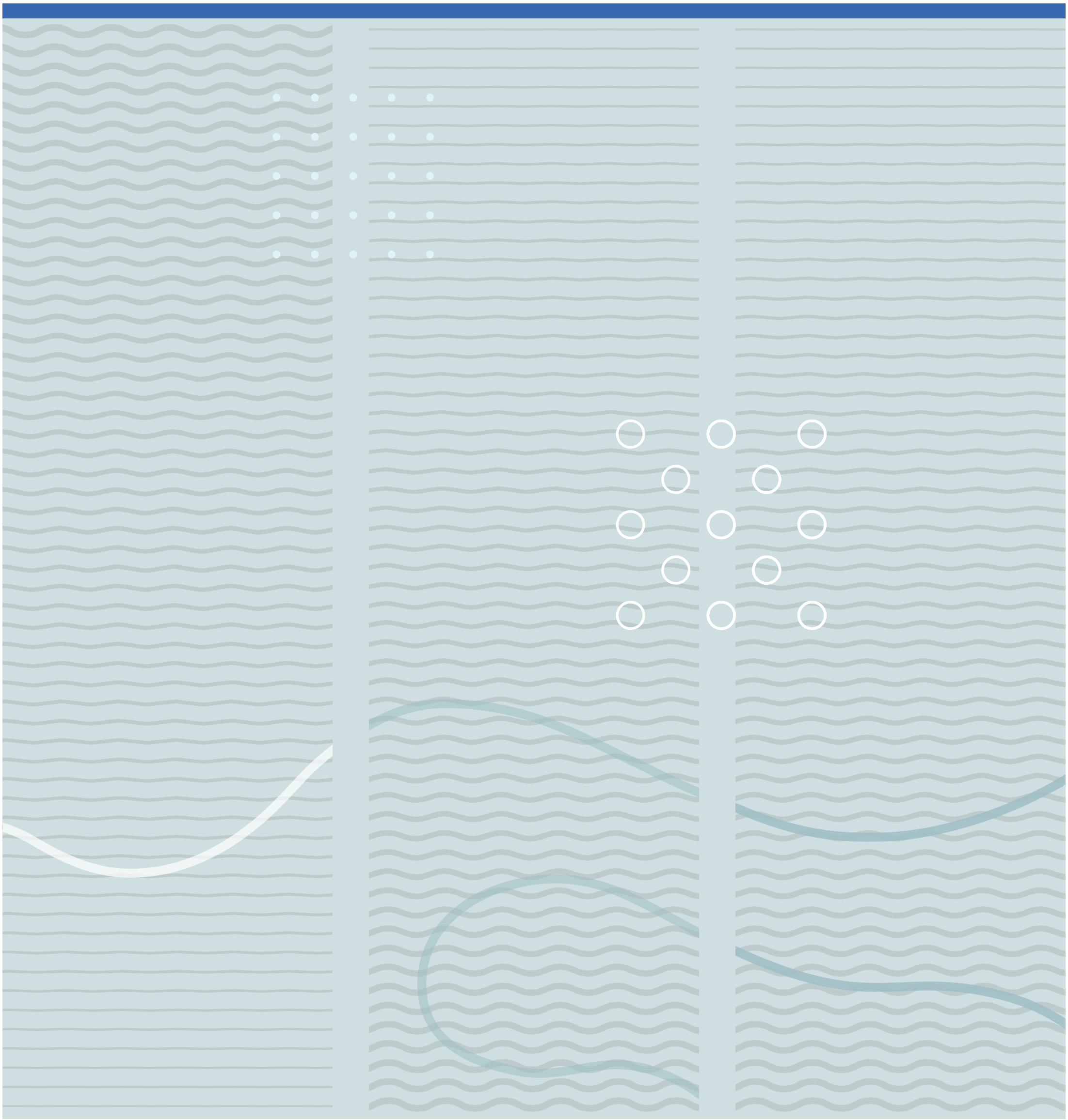

Uyen Phuong Do

Glucose energy harvester for self-powering of remote distributed bioanalytical microsystems

A PhD dissertation in
Applied micro- and nanosystems

© Uyen Phuong Do, 2021

Faculty of Technology, Natural Sciences and Maritime Studies
University of South-Eastern Norway
Horten, 2021

Doctoral dissertations at the University of South-Eastern Norway no. 88
ISSN: 2535-5244 (print)
ISSN: 2535-5252 (online)

ISBN 978-82-7860-465-6 (print)
ISBN 978-82-7860-464-9 (online)

This publication is licensed with a Creative Commons license. You may copy and redistribute the material in any medium or format. You must give appropriate credit, provide a link to the license, and indicate if changes were made. Complete license terms at https://creativecommons.org/licenses/by-nc-sa/4.0/deed.en

Print: University of South-Eastern Norway

Dedication

To my family

my parents, my husband (Duy-Son Nguyen),

my children (Daniel Nguyen and Selena Nguyen).

Preface

This doctoral thesis is submitted for the degree of Doctor of Philosophy at the Faculty of Technology, Natural and Maritime Sciences, University of South-Eastern Norway (USN). The work was carried out between August 2010 and December 2016 (including a 2 years maternity leave) at the Department of Microsystems (USN) under the supervision of Prof. Erik Andrew Johannessen, Prof. Kaiying Wang and Prof. Øivind Johannesen. Significant contributions were also made by Prof. Frode Seland at the Norwegian University of Science and Technology (NTNU).

This work is financially supported by the Norwegian Ministry of Education and Research (KD) program at University of South-Eastern Norway, and the Norwegian Ph.D. Network on Nanotechnology for Microsystems (221860/F40).

Acknowledgements

This project has been developed at the Department of Micro Systems (IMS) at the University of South-Eastern Norway (USN). I would like to thank the Norwegian Ministry of Education and Research (KD) program at University of South-Eastern Norway for the financial support as well as the Norwegian Ph.D. Network on Nanotechnology for Microsystems (Nano Network) and the Norwegian Micro- and Nanofabrication facility (NorFab) for their funding contributions.

First and foremost, I am deeply grateful to my supervisor, Professor Erik A. Johannessen. His guidance, motivation, support and patience both in technical and non-technical matters were essential for the completion of this work. I want to thank to my co-supervisors, Professor Kaying Wang and Professor Oivind Johannessen, for their supports. I also express my sincere thanks to the significant contribution from Professor Frode Seland at the Norwegian University of Science and Technology (NTNU). I would like to thank Professor Michel M. Maharbiz at Berkeley Sensor & Actuator Center (BSAC), the University of California, Berkeley, USA for the collaboration during my student exchange period.

I would like to give sincere thanks to Ragnar D. Johansen, Thomas Martinsen, Zekija Ramic and other lab engineers for their help and support for my experimental work. A special thank you note is from me to Luis Andre L. Fernandes and other BioMEMS group members at IMS for their useful presentations and discussions.

At last but not least, I am thankful to my Vietnamese friends in USN. Without you, the winter in Norway would be colder. Finally, I want to send a special appreciation to my parents, my husband and my children. They are the biggest motivators and supporters for me to this far in my academic journey.

Declaration

I hereby declare that all material presented in this thesis is my own research unless otherwise stated.

Abstract

Implantable medical devices came of age with the artificial pacemaker more than 60 years ago. Their true potential of being located directly where their prosthetic or therapeutic actions are needed will be further enhanced by making them smaller with the aid of microfabrication. Their Achilles heel comes at the cost of limited lifetimes of an otherwise functional unit due to their small footprint limiting the size and energy storage capacity of current power supply solutions based on batteries. In contrast, chemical energy harvesters based in exogeneous fuels such as glucose and dissolved oxygen may hold the best promise of developing a long-term energy supply due to the relative abundance of these fuels *in vivo*.

This thesis focuses on the development of such a chemical energy harvester. Based on the depletion design published in prior art, the quest has been to design a glucose fuel cell with electrodes and catalysts that are compatible with thin film microfabrication. These are mounted as a stacked assembly where one of the electrodes is made as a novel porous cathode through which the reagents diffuse and the initial separation of reagents takes place.

The first challenge of making an electrode for the selective reduction of oxygen was realised by developing a porous cathode from e-beam deposition of palladium thin films on ceramic aluminium oxide substrates. The porous nature of the cathodes improved the catalytic properties by increasing the real surface area close to 100 times of the geometric surface area. It yields an exchange current density of $2.9 \times 10^{-3} \pm 0.5 \times 10^{-3}$ µA cm^{-2} at a dissolved oxygen concentration close to the physiological range of 2 ppm. The sensitivity towards glucose was assessed by measuring the decrease in the half-cell potential in the presence of 5 mM glucose to $- 20.6 \pm 16.1$ mV under a load current density of 2 µA cm^{-2}. The Tafel slopes were measured to approximately 60 mV per decade. These results suggested that nanoporous AAO cathodes coated with palladium offered a reasonable catalytic performance with a good selectivity towards oxygen in the presence of glucose.

The second challenge of realising selective oxidation of glucose started off by developing glucose selective anodes from the annealing of e-beam deposited thin films of platinum (Pt) and nickel (Ni) into a Pt– Ni alloy. The roughened surface of the alloy enhanced the electrochemical properties by increasing the real surface area to approximately 500 times compared to the geometric surface area. Since the surface roughness was found to scale with the annealing temperature, the corresponding exchange current density of the electrodes annealed at 800^{o}C was twice that of the electrode annealed at 650^{o}C. The potential increase due to the addition of dissolved oxygen at the physiological concentration of 2 ppm was measured to 100 ± 8 mV under a load current density of 2 µA cm^{-2}. These results showed that the anodes are relatively more sensitive to oxygen catalysis than the cathodes towards glucose catalysis. It suggested that a shield should be made to remove the oxygen before permitting the solution to come into contact with the anode.

Consequently, the third challenge of completing a selective oxidation of glucose and a selective reduction of oxygen lies in the architecture of the fuel cell device. A custom housing enabled a stacked assembly of the fuel cell “core” meaning the anode at the bottom, covered by an ion conducting membrane, and capped with the cathode, showed that energy harvesting from a mixed fuel environment was possible. In fact, the cell was able of maintain a power density of 2.33 ± 0.11 µW cm^{-2} at a current density of 7.7 µA cm^{-2} and a cell potential of 0.30 ± 0.01 V in a simulated mixed fuel environment of 5 mM glucose and 2 ppm dissolved oxygen at room temperature. This was 80% of the power obtained in the ideal experiment in which glucose and oxygen were physically separated prior to use.

It was also found that the methods used to estimate the real surface area of nanoporous electrodes were not thoroughly discussed in literature. Although this may be clear to those already skilled in the art, mistakes can be done by those coming from a different engineering background. Thus a subsequent study investigating different popular *ex-situ* and *in-situ* methods was undertaken to help clarify this matter and to identify the correct methods used for the electrode systems developed in this project.

List of publications

Articles omitted from online publication due to publisher's restrictions

Article I

Do, U.P., Seland, F., Maharbiz, M.M., Wang, K., Johannesen, Ø., Johannessen, E.A. Thin film nanoporous electrodes for the selective catalysis of oxygen in abiotically catalysed micro glucose fuel cells. Journal of Materials Science. 2016. 51 (19): pp. 9095-9107.

Article II

Do, U.P., Seland, F., and Johannessen, E.A. The Real Area of Nanoporous Catalytic Surfaces of Gold and Palladium in Aqueous Solutions. Journal of the Electrochemical Society, 2018. 165 (5): H219-H228.

Article III

Do, U.P., Seland, F., Wang, K., and Johannessen, E.A. Raney-platinum thin film electrodes for the catalysis of glucose in abiotically catalyzed micro-glucose fuel cells. Journal of Materials Science, 2019. **54** (22): pp 14143–14156. DOI: 10.1007/s10853-019-03907-9

Article IV

Do, U.P., Seland, F., and Johannessen, E.A. A micro fuel cell for abiotical catalysis of glucose. Journal of Power Sources, 2020. **478**: p. 229032. DOI: 10.1016/j.jpowsour.2020.229032.

List of tables

Table 2-1: Key features of implantable µGFC 19

Table 2-2: Highlights of the main achievements in the development of enzymatic µGFC. 22

Table 2-3: Highlights of the main achievements in microbial µGFC development 25

Table 2-4: Highlights of the main achievements in abiotical µGFC development since 1967 29

List of figures

Figure 1-1: Some examples of implantable medical devices and their functions [18].....2

Figure 1-2: Current power supplies for implantable medical devices (a) Single use lithium battery [16] (b) photovoltaic cell [31] (c) ultrasonic power transducer [18] (d) magnetic induction energy transfer [18] (e) capacitive coupling [44] (f) coiled-up thermoelectric power generator [16] (g) kinetic energy harvester from heart contractions [45] (h) micro enzymatic glucose fuel cell in *ex vivo* human blood vein replica [46] 8

Figure 1-3: Comparable power densities of the different types of power supplies considered for use in implantable medical devices. [18, 49, 52, 80, 83-84] 16

Figure 2-1: Example of chemical reaction with GOx as anodic catalyst, multicopper oxidases as cathodic catalyst and electron transfer mediator [94]. 20

Figure 2-2: An example of the chemical reactions occurring inside a microbial µGFC using *S. Cerevisiae* [104]........23

Figure 2-3: Three main designs of the abiotic µGFC intended for tissue implantation: (a) bifacial access to the anode and cathode [115] (b) single layer fuel cell with access from one face [121] (c) depletion (stacked) design using membranes to separate/reduce the flow of a specific reagent to the respective electrodes (i)[124] (ii)[110] 32

Figure 3-1: The AAO membranes were held in place during the metal deposition process using a custom holder that permitted (a,c) positioning in “pockets” located in the base, on which a lid was attached (b,d) to prevent them from coming loose. 41

Figure 3-2: As prepared electrode ready for use. 43

Figure 3-3: (a) Schematic representation of the fuel cell assembly (b) stacked fuel cell assembly (i) whole piece (ii) cross section 44

Figure 3-4: Experiment set-up with a U-tube cell. The shaded area corresponds to PBS buffer acting as both electrolyte and media for glucose and DO storage. 48

Figure 3-5: Circuit models used to fit the EIS analysis for electrodes (a) cathode (b) anode. 49

Figure 4-1: CVs showing the oxidation of iodine-adsorbed to (a) Pd and (b) Au electrodes with 100 and 200 nm pores. 53

Figure 4-2: CVs of the (a) Pd electrodes and (b) Au electrodes with 100 and 200 nm pores. The arrow shows the scan direction. 54

Figure 4-3: EIS curves of (a) the Pd electrodes and (b) the Au electrodes. The equivalent circuit for fitting the data of both electrodes is shown in inset (i). The full extension of the EIS curves from the Au electrodes is shown in inset (ii) is. The alternative equivalent circuit for fitting the data of the Au electrodes is shown in inset (iii). 55

Figure 4-4: Comparative analysis of the different methods used to determine the real surface area. The black bar on the center top surface of the columns represents the standard error of the mean (n = 3 number of measurements). 56

Figure 4-5: Deposition of metal clusters inside the pore rim of the AAO membrane substrate (arrows) with 200 nm pore size for (a) 100 nm thick Ag and (b) 200 nm thick Pd. The Ag was used as a test material before choosing Au and later Pd as the catalyst. 60

Figure 4-6: Surface architecture of the thin film Raney-Platinum alloy after fabrication annealed at (a) 650°C and (b) 800°C. The inserts show the EDS for the respective electrode surfaces. 62

Figure 4-7: Polarization curves obtained from the fuel cell representing (a) the best scenario with separate fuels at the anode and cathode; (b) the worst scenario in which both reagents are mixed, and (c) using a stacked fuel cell assembly attempting a separation of the fuels in a mixed fuel environment. The error bars correspond to ± 1 std dev, n = 3 number of measurements. 64

Abbreviations and Symbols

σ	Conductivity
$[Fe(CN)_6]^{4-/3-}$	Hexacyanoferrate (II/III)
µGFC	Micro Glucose Fuel Cells
3D	Three dimension
AAO	Aluminum Oxide
AC	Alternating current
AEM	Anion Exchange Membranes
AFM	Atomic Force Microscopy
Ag	Silver
A_{geo}	The geometric surface area
Al	Aluminum
A_{real}	The real area
ASR	The area specific resistance
Au	Gold
Bi	Bismuth
$C_6H_{12}O_6$	Glucose
$C_6H_{12}O_7$	Gluconic Acid
CEM	Cation Exchange Membranes
CF_x	Carbon mono-flouride
CMOS	Complementary Metal-Oxide Semiconductor
CNT	Carbon Nanotubes
CO_2	Carbon dioxide
Cu	Copper
CUT	Capacitive Ultrasonic Transducer
CV	Cyclic Voltammetry
DC	Direct current
DLC	Double layer capacitance measurement
DO	Dissolved Oxygen
e^-	Electrons
EDS	Energy Dispersive X-Ray Spectroscopy
EIS	Electrochemical Impedance Spectroscopy
FDA	U.S. Food and Drug Administration
FE	Hexacyanoferrate (II/III) electrocatalysis
f_r	Roughness factor
GOx	Glucose Oxidase
H^+	Proton
H_2O	Water
H_2SO_4	Sulfuric Acid
I_2	Iodine
IA	Iodine adsorption
IR	Infrared
Ir	Iridium

j_0	Intrinsic exchange current density
j_0*	Effective exchange current density
Li	Lithium
MEMS	Mechanical Electrical Micro Systems
MnO_2	Manganese oxide
NADH	Nicotinamide Adenine Dinucleotide
Ni	Nickel
O_2	Oxygen
OF	Oxide formation
OH^-	Hydroxide Anion
Pb	Lead
PBS	Phosphate-Buffered Saline
Pd	Palladium
PdO	Palladium Oxide
PEEK	Polyetheretherketone
PEM	Proton Exchange Membranes
Pt	Platinum
PTFE	Polytetrafluoroethylene
PUT	Piezoelectric Ultrasonic Transducer
Q_{tot}	the total charge obtained in the iodine containing electrolyte
Q_{bg}	the background charge obtained in the iodine free electrolyte
Q_{iod}	the charge from the oxidation of the adsorbed iodine at the electrode
Redox	Reduction-Oxidation
Rh	Rhodium
SEM	Scanning Electron Microscopy
$SOCl_2$	Thionyl chloride
Supor 450	Polyethersulfone
SVO	Silver vanadium oxide
Ti	Titanium
U^o	Standard potential
Zn	Zinc
ZnO	Zinc Oxide
ΔG^o	Gibbs free energy

Table of contents Page

Dedication ... III
Preface ... V
Acknowledgements ... VII
Declaration ... IX
Abstract ... XI
List of publications ... XIII
List of tables ... XV
List of figures ... XVII
Abbreviations and Symbols ... XIX
Table of contents ... XXI

1. Introduction ... **1**
- 1.1. Motivation ... 1
- 1.2. Current power sources for implantable medical devices ... 6
  - 1.2.1. Single-use batteries ... 6
  - 1.2.2. Power transferring mechanisms for rechargeable batteries ... 9
  - 1.2.3. Energy harvesters ... 12

2. Micro glucose fuel cells ... **17**
- 2.1. Operation principle ... 17
- 2.2. Classification of µGFC based on the catalysts ... 19
  - 2.2.1. Enzymatic µGFC ... 19
  - 2.2.2. Microbial µGFC ... 23
  - 2.2.3. Abiotic µGFC ... 26
- 2.3. Construction consideration and challenges of µGFC ... 26
- 2.4. Implantable abiotically catalysed glucose fuel cells ... 28
  - 2.4.1. Historical development ... 28
  - 2.4.2. State of art of designs ... 32
  - 2.4.3. State of art of construction ... 34

3. Materials and Methods ... **39**

3.1. Electrode fabrication 39
  3.1.1. Nanoporous oxygen selective Pd cathodes 39
  3.1.2. Raney Pt-Ni anodes 41
3.2. Sample preparation 42
  3.2.1. Electrodes 42
  3.2.2. Fuel cell 43
3.3. Determination of the real surface area 44
  3.3.1. Consideration of real area vs. geometrical area 44
  3.3.2. Nanoporous oxygen selective cathodes 45
  3.3.3. Raney Pt-Ni anodes 46
3.4. Performance 46
  3.4.1. Electrodes 46
  3.4.2. Fuel cell 47
3.5. Electrochemical impedance spectroscopy (EIS) 48

4. Results and discussion (summary of articles) 51
4.1. Determination of the real surface area 51
  4.1.1. The Real Area of Nanoporous Catalytic Surfaces of Gold and Palladium in Aqueous Solutions (Article II) [30] 51
  4.1.2. Nanoporous oxygen selective Pd cathodes (Article I) 56
  4.1.3. Raney Pt-Ni anodes (Article III) 57
4.2. Performance 57
  4.2.1. Thin film nanoporous electrodes for the selective catalysis of oxygen in abiotically catalysed micro glucose fuel cells (Article I) 57
  4.2.2. Raney-platinum thin film electrodes for the catalysis of glucose in abiotically catalysed micro-glucose fuel cells (Article III) 61
  4.2.3. A micro fuel cell for abiotical catalysis of glucose (Article IV) 63

5. Conclusion and future work 65
5.1. Conclusion 65
5.2. Future work 67

References 71

Collection of Articles 81

1. Introduction

1.1. Motivation

The growing number of older people in a world combined with a rise in life expectancy will most likely raise the prevalence of age related chronical medical diseases. Factoring in an industrialized lifestyle in addition with less mobility and a diet that is increasingly dependent on sugar and fat related products may further enhance the susceptibility of contracting age-related diseases at a younger age. This will increase the burden of an already overstretched health system to a level that may no longer be sustainable. One possible solution that may alleviate this negative trend of cost versus care may be the onset of miniaturized and low cost (implantable) medical devices. These may monitor or treat a medical condition in real time, and thereby intervene at an early stage of disease progression and thus prevent complications that otherwise would have resulted in costly hospitalization and rehabilitation. Implantable medical devices have already made their impact as shown in Figure 1-1, with a global market share of 96.6 billion USD in 2018 [1], and a forecasted growth of more than 10% by 2025 following the trend of the cardiac defibrillator [2].

The field of implantable medical devices has taken advantages from the developments in materials, biotechnology and microelectronics over the past six decades. This can be clearly seen in the technological development that has taken place from the first report on electrical heart stimulation by Zoll in 1952 [3]. This was followed by the invention of the implantable heart pacemaker by Senning and Elmqvist in 1958 [4] leading to modern leadless pacemakers such as the Micra Transcatheter Pacing system that received FDA approval in April 2016 [5]. Demands and preferences of the patients affect heavily on the design of implantable medical devices. In general, the smaller the implants are made, the less intrusive it is to normal human activity and will consequently offer a better quality of life to the patients. In this respect, the largest single component that restricts miniaturization is the power supply unit. For example, more than half of the weight and volume of a cardiac pacemaker is occupied by the power supply (i.e. battery) [6]. This factor can be reduced at the cost of device lifetime, but performing surgery to remove or replace the power supply unit is not a desirable proposition. Hence, alternative power supplies that rely on the transfer or harvesting of energy from an external source have been considered as potent new candidates.

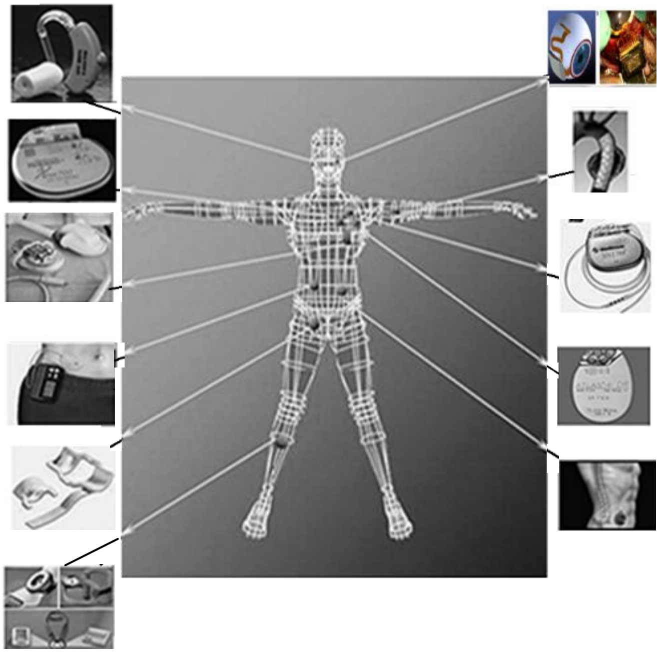

Cochlear implants: **Restore hearing [7]**

Pacemaker: Restore irregular heart rhythm [9]

Artificial heart: Organ replacement [11]

Insulin pump: insulin injection on demand [13]

Incontinence device: treat spasticity urinary tremor control [15]

Bone growth stimulators: Heal bone fracture [17]

Retinal implants: Restore vision [8]

Vascular grafts: Reconnect blood vessels [10]

Neuro stimulators: Relieve chronic pain [12], muscle movement

Cardiac defibrillator: Prevention of sudden death [14]

Drug pump: Supply drugs when needed or continuously [16]

Figure 1-1: Some examples of implantable medical devices and their functions [18]

This project focuses on research aspects utilizing glucose and oxygen, which are abundant in the human body, as renewable energy sources to power implantable medical devices. These chemical fuels technically constitute an unlimited supply of reactants taking into account the size, volume and power requirement of a human being compared to that of a tiny electronic implant. The power conversion takes place with help of fuel cell technology and some selected challenges of the implantable micro glucose fuel cells (µGFC) working in the physiological solution of the body have been addressed. The most important feature as well as differences from more conventional hydrogen fuel cells is that the chemical fuels or reactants utilized by µGFC exist as a mixture in body fluids in contrast to separate reagents of hydrogen and oxygen. The simultaneous presence of glucose and oxygen at both the cathodic and anodic electrodes could result in an electrochemical short-circuit triggering the formation of mixed potentials at electrodes which cause no net electricity production. Therefore, the separation of glucose and oxygen from this mixture is a key challenge.

The separation challenge has revolved around the concept of removing one of the fuels (reactants) at the first electrode before passing the second reactant to the other electrode mounted below in a kind of stacked fuel cell assembly. This idea was first introduced by Rao *et. al.* [19] in 1974. He created a depletion region in the cell by mounting a cathode consisting of oxygen sensitive but glucose insensitive catalysts in front of the anode. By removing oxygen in this manner, he was able to create anoxic conditions at the glucose sensitive (and oxygen sensitive) anode. However, pure oxygen selective catalysts, which are the most important part of this design, haven't yet been found in the literature. Thus, a lot of efforts have been made on the use of Platinum (Pt) or Pt type alloys in order to reach this goal. Alternative catalysts made of palladium (Pd) offers similar qualities to that of Pt, and selective properties towards oxygen reduction have been investigated in acid and alkaline media [20-22]. However, Pd hasn't received enough attention on its selective properties towards oxygen reduction in neutral physiological solutions (pH 7.4), particularly in the presence of glucose.

Research Question

This project will seek to investigate the oxygen selective properties of Pd in neutral physiological solutions in the presence of glucose. The catalyst will be made from thin film layers compatible with current microfabrication methodologies, which pose a challenge increasing the effective surface area (roughness factor) due to limited vertical dimensions. The thicknesses of electrodes based on Pt alloys have normally been in micrometer-range [23], with the exception from some thin film studies performed in later years [24]. The challenge with limited surface roughness was resolved by combining thin film deposition with substrates made from commercial porous alumina (AAO) membranes. These have not received too much attention in spite of offering favourable characteristics such as pores through which glucose can pass, a three-dimensional surface morphology that increases surface roughness of the thin film catalyst, commercial availability, small size and adaptability towards microfabrication technologies. The glucose selective catalyst made of Pt-Ni alloy will be deposited on a flat non-porous substrate to explore to what extend an increase in surface roughness is possible with thin films that are alloyed and subsequently etched to create the 3D topography. This alloy was also tested in a simulated physiological condition in the presence of oxygen (and glucose) similarly to the Pd cathode.

After characterizing the properties of Pd and Pt-Ni alloys, both electrodes will be combined in a stacked layered fuel cell reminiscent of that designed by Rao. Thus, would this combination of thin film catalysts and microfabrication compatible substrates permit oxygen to be scavenged at the cathode to such a degree that the anode resides in an anoxic environment capable of generating a comparable power from glucose and oxygen that that reported in literature?

This resulted in the formulation of the following three research objectives:

1. The development of an oxygen scavenging porous cathode: The fabrication and characterization of the cathode is presented in Article I [25]. A nanoporous cathode was fabricated by fine tuning the pore size of a commercial aluminium oxide membrane which acts as substrate / electrode carrier for the deposition of the oxygen selective catalyst. The active surface area and the catalytic activity at different concentrations of oxygen and glucose were characterized.

2. The development of a glucose selective anode: The fabrication and characterization of the anode is presented in Article III [26]. Since the catalytic activity of the anode would tail the cathode, a process was implemented to roughen the thin film catalyst to increase its surface area. Given a constant catalytic activity per unit area, the net current generated would scale with the surface area of the electrode.

3. The assembly and the characterization of the µGFC, presented in Article IV [27]: The nanoporous oxygen selective cathode and the roughened glucose-selective anode were assembled in a stacked fuel cell assembly, and characterize under simulated physiological conditions.

In the electrochemistry field, a large real active surface area for the chemically reactive sites could give the impression of a more active catalyst compared to a smoother surface of the same material and could consequently improve the catalytic performance of the electrodes having a small geometric area. The large active surface area usually comes from the micro- and nano-topographic structures and trenches that are only visible on the microscopic scale [28-29]. Most of the kinetic parameters published in the electrochemical field are referred to the geometric surface area [28-29]. Therefore, the determination of the real surface area plays an important role in the determination of the catalytic behaviour of a given catalyst. As reported by other groups, a lot of experiment methods for surface area determination of Pt electrodes have been reported in literature [28-29]. However, no universal methods that can be applied to any electrode material are available. This is an area where the choice of methods may not be suitable for a given material or where the geometry may give erroneous results if the users are not aware of this. Gold (Au) and Pd are commonly used as the replacement for Pt but not suitable for all surface area determination methods used for Pt. Therefore, one part of this project was dedicated the investigation of different methods available for the determination of the real surface area of the Au and Pd electrodes (Article II) [30].

1.2. Current power sources for implantable medical devices

Current power supply technologies suitable for implantable medical devices can be categorized into (i) single-use batteries, (ii) rechargeable batteries with power transferring mechanism or (iii) energy harvesters, based on thermoelectricity, kinetic (electrostatic, electromagnetic energy generator) [31-32] as well as electrochemical cells such as the one explored in this project. Some of the examples are shown in Figure 1-2 and their power densities are compared in Figure 1-3.

1.2.1. Single-use batteries

Since the first battery was invented by Volta in 1796, numerous types have been developed and employed by humans [18]. As shown in Figure 1-2.a, the energy in batteries is stored in the electrolyte which can undergo an electrochemical reaction with two electrodes to produce electricity. The typical single-use power supply used in implantable medical devices is the Lithium (Li) battery which shares a common anodic electrode of solid Li metal. In contrast, there are several choices of cathodic electrodes: solid iodine (also denoted Li/I_2 batteries) [18, 33-34], manganese oxide (Li/MnO_2) [18, 35-36], carbon mono-flouride (Li/CF_x) [18, 37-38], silver vanadium oxide (Li/SVO) [18, 39-40], thionyl chloride ($Li/SOCl_2$) or hybrid cathodes that consist of a combination of different element (Li/CF_x-SVO) [18, 41-43]. $Li/SOCl_2$ and Li/CF_x ;batteries have a track record for use in neuro-stimulators and drug delivery [18]. Among those, Li/I_2 batteries have been frequently employed in implantable pacemakers during the past 40 years. The reason for this is that they have a high energy density of up to 210 W·h/kg combined with a low self-discharge rate [18]. They also provide stable voltages through their operational lifetime and a predictable gradual decrease in voltage at the end, which provide a useful signal that can be used to schedule a timely replacement of the battery [6]. Although such single-use batteries have been widely applied in implantable medical devices, their main disadvantage is still that they have to be replaced by surgery with the added danger of infection and a renewed inflammation at the implantation site, in addition to the cost of surgery and the recovery/healing process.

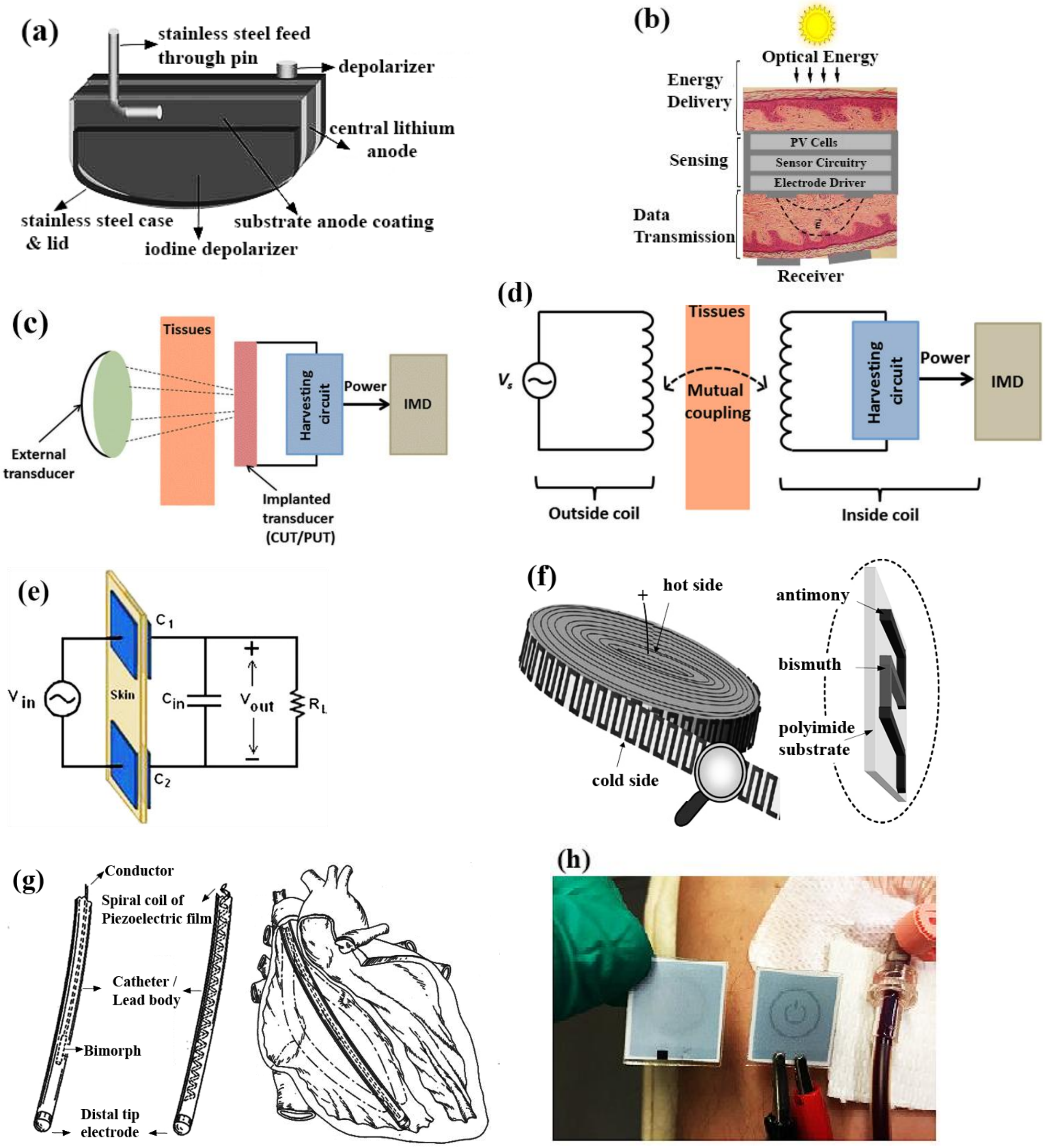
(a)
stainless steel feed through pin
depolarizer
central lithium anode
stainless steel case & lid
substrate anode coating
iodine depolarizer
(b)
Optical Energy
Energy Delivery
Sensing
PV Cells
Sensor Circuitry
Electrode Driver
Data Transmission
Receiver
(c)
Tissues
Harvesting circuit
Power
IMD
External transducer
Implanted transducer (CUT/PUT)
(d)
V_s
Tissues
Mutual coupling
Harvesting circuit
Power
IMD
Outside coil
Inside coil
(e)
C_1
V_{in}
Skin
C_{in}
V_{out}
R_L
C_2
(f)
+
hot side
cold side
antimony
bismuth
polyimide substrate
(g)
Conductor
Spiral coil of Piezoelectric film
Catheter / Lead body
Bimorph
Distal tip electrode
(h)

Figure 1-2: Current power supplies for implantable medical devices (a) Single use lithium battery [16] (b) photovoltaic cell [31] (c) ultrasonic power transducer [18] (d) magnetic induction energy transfer [18] (e) capacitive coupling [44] (f) coiled-up thermoelectric power generator [16] (g) kinetic energy harvester from heart contractions [45] (h) micro enzymatic glucose fuel cell in *ex vivo* human blood vein replica [46]

1.2.2. Power transferring mechanisms for rechargeable batteries

The limited lifetime of single-use batteries has raised awareness of systems based on wireless power transfer from an external supply that is capable of transmitting energy directly to energy storage units (rechargeable batteries or super capacitors) in the medical implant. The energy can be transmitted through body tissues by some means of radiation such as optical, ultrasound, electro-magnetic or electrostatic.

1.2.2.1. Optical energy transfer

Optical energy can be transmitted through a laser diode in the near-infrared (near-IR) or IR region towards an array of photovoltaic cells integrated under the skin (Figure 1-2.b) [18, 47-48]. The photovoltaic cell array converts the received radiation into electric currents. Based on the wavelength, the radiation may access deep inside biological tissues. One study reported the use of such a photovoltaic cell array with a surface area of 2.1 cm^2 embedded under the abdominal skin of a rat. Optical energy transfer was initiated by illuminating near-IR light through the skin with a thickness of 0.8 mm [49]. This power supply was able to provide energy for a cardiac pacemaker (which consumes 20 µA) for 24 hours from a 17-minute charging time at a charge current of 1.7 mA from a near-IR source transmitting at 810 nm and a power density of 22 mW cm^{-2} [18, 49]. Although the light typically has low interactivity with biological tissues, the laser irradiation used in this particular study could raise the skin temperature by 2.2^oC during the charging period [49]. Moreover, the requirement of a relatively “large” size (2.1 cm^2 for the surface area of the photovoltaic cell array [49]) and a low power conversion efficiency (9.5% in a device implanted in a mice [50]) are some of the drawbacks of this method [18].

1.2.2.2. Ultrasonic energy transfer

Externally transmitted ultrasonic waves can be utilized by an ultrasonic transducer embedded in the implant (Figure 1-2.c). This transducer converts the incident sound waves into an electrical potential through a change in capacitance (using a capacitive ultrasonic transducer - CUT) or through the piezoelectric effect (piezoelectric ultrasonic transducer - PUT) [51-52]. The first implantable ultrasonic power supply was reported by Cochran in 1988, and measured 0.5 x 0.5 x 0.09 cm [18, 52]. This implant was based on a piezoelectric ceramic transducer that was located in the anterior surface of the femur of laboratory-bred beagles. The transducer was shown to generate an output power of 1.5 mW cm^{-2} from an input potential of 10 – 20 V and a frequency of 2.25 MHz [18, 52]. In general, the low-frequency of the ultrasound waves (usually in the range of 2.5 – 7.5 MHz) are able to penetrate deep into the human body (beyond 3 cm from the skin surface) but with a poor focus point meaning that the energy is dispersed over a larger area. In contrast, high-frequency ultrasound waves (usually in the range of 7.5 – 15 MHz) could focus on a selected area but are limited to a penetration depth of 3 cm [16, 18, 53-54]. This technology benefits from the compact size of the device (the piezoelectric ceramic transducer has a footprint of only 0.25 cm^2 [52] compared to that of the photovoltaic cell array of 2.1 cm^2 [49]). The transducers are based on MEMS technology, and it is easy to tailor a specific operating wavelength. Moreover, the use of ultrasonic power is considered safe with a relatively high transmission efficiency of 10-15% [18, 55]. In spite of these advantages, the ultrasonic power transfer technology still faces some challenges. Ultrasound waves may cause physical pain and potential tissue damage due to the conversion of mechanical energy into heat and through the process of cavitation (the formation of gas bubbles high / low pressure zones that collapses and cause tissue damage) [56].

1.2.2.3. Magnetic induction energy transfer

The invention of wireless power transfer by magnetic induction in 1831 by Michael Faraday and the first report of wireless power / data transfer by Tesla in 1914 paved way for the concept of inductive power transmission of implantable medical devices [18, 57]. The power is transferred through a mutual inductive coupling link based on a pair of coils / antennas, where the primary coil is positioned externally in direct contact with the skin and the secondary coil was implanted under the skin (Figure 1-2.d). The external primary coil will upon powering from an AC source generate an alternating magnetic field that penetrates and induce a current in the (implanted) secondary coil [32]. Most studies related to such inductive links have used frequencies below 20 MHz to avoid excessive absorption of the radiation and consequently tissue heating [44, 58-59]. Inductive power transfer has normally been limited to a few centimeters due to the rapid fall of transmitted power with distance [60]. However, a research group proved that even with a small coil of 10 x 13 mm^2 located in an endoscopic capsule, power transfer was possible over a distance of up to 20 cm from an external source of 150 mW running at 1 MHz [61]. The efficiency of this wireless power transfer relies on the resonance frequency, operating frequency, working distance, coil size, orientation and alignment between the transmitter and the receiver coils [18, 62-64], but is rarely above 1 % [65].

1.2.2.4. Capacitive coupling link

Unlike power transfer with magnetic fields, capacitive coupling uses electric fields as the carrier for power and data. Although this approach has been employed for inter-chip data communication and even for power transfer for short wireless communication, only a few studies exit for implantable biomedical applications since the first report were issued in 2009 by Sodagar *et. al.* [44, 66-67]. In this method, a capacitive coupling is created between an external plate mounted on the skin surface, and a second plate implanted parallel to the first one below the skin surface (Figure 1-2.e). The skin and thin tissue layers located in between these two plates acts as the dielectric. In order for this setup to work, a second set of one external and one implanted plate is positioned nearby and parallel to the first pair. An AC potential applied to the two external plates will create a DC potential between the two implantable plates. This DC potential can then be used to supply energy to an implantable load (battery or supercapacitor). In 2010, Asgarian *et. al.* demonstrated the potential transfer rate close to 1 was possible with plates measuring only 2 x 2 mm^2, and with a separation of 3 mm assuming the dielectric properties of dry skin [68]. The electric fields carrying energy with this method are well confined within the area restricted by the capacitive plates. This may reduce or even eliminate the electromagnetic interference on sensitive analog circuitry in the implantable system [68]. It is also compatible with standard CMOS processing technologies easing the production protocol upon implementation in microsystems design. The main drawback of capacitive coupled power transfer is again the possibility of localized increase in the temperature at the skin tissue interface during the charging period [44].

1.2.3. Energy harvesters

Energy harvesting devices generate electric energy from their surroundings by means of some energy conversion mechanism. The consensus is that implantable devices powered by this manner may exhibit extended lifetimes since they no longer rely on the limited capacity of the battery. Consequently, scavenging energy from humans may represent an interesting alternative for implantable medical devices. Humans can be a good source of kinetic, thermal and chemical energies. Thus, many researchers have proposed various useful energy scavenging solutions in this respect [18, 69-73].

1.2.3.1. Thermal energy generator

Although the core temperature of the human body revolves around 37°C, there are regions of variable temperatures ranging from the underlying tissue to the skin surface and from the torso to the extremities such as hands, feet and head, as well as the temperature differences between the skin and ambient air. Most energy scavengers based on temperature gradients are placed either in contact with the skin or implanted just below the skin surface. They utilize the Seebeck effect in which a potential difference across a thermos-electric module, consisting of one or multiple thermocouples connected in series, scales with the applied temperature gradient [18, 73]. A thermocouple is a device that is made from two dissimilar metals with different Seebeck coefficients. The Seebeck coefficient is the potential difference that appears on either end of the conducting material when one end is heated up relative to the other. The physical mechanism behind this behaviour will not be discussed here, but is related to the organization and density of electrons relative to the temperature for a given material. By considering a temperature difference between the skin surface of 34^{o}C and the air temperature of 22^{o}C (8 K) a theoretical maximum of 180 μW cm^{-2} can be generated from a heat flow of 20 mW cm^{-2} [74]. However, the effective temperature gradient will be much smaller due to the presence of thermal contact resistance and low convective cooling on the cold side. In 1999, Stark *et. al.* introduced thin film produced 0.19 cm^{3} thermoelectric generator with a density of 11.9 thermocouples mm^{-3} that were able to generate a potential of 1.1 volts and an output current of 1.4 μA at a temperature gradient of 5 K, increasing to 2.1 V and 2.8 μA at 10 K. This corresponds to a power of 1.5 and 5.8 μW respectively, [18, 75]. A commercial wearable prototype, proposed by Thermo Life® in 2006, had a volume of 0.1 cm^{3} and a weight of 0.23 g. This unit could generate up to 2.6 V, 11 μA and a power of 28 μW from a temperature gradient of 5 K [76]. The relatively small thermal gradients in the human body makes it difficult to achieve significant power outputs, and thus a large number of thermocouples would need to be cascaded in an appropriate way at the expense of an increase in the size [18, 73].

1.2.3.2. Kinetic energy generator

Energy scavengers from kinetic energy use the inertial force of a proof mass as the input for power scavenging through three main transduction mechanisms: electromagnetic, electrostatic and piezoelectric [44, 69]. In the electromagnetic transduction, the relative motion of a magnet, normally serving as a proof mass, and a coil, normally stationary, causes a time varying magnetic flux density through the coil to produce energy [77]. The electrostatic transduction is based on a pre-bias capacitance varying with an inertial mass movement [77]. The piezoelectric transduction is based on piezoelectric materials which generate proportional electrical polarization with respect to the applied mechanical stress [18]. The practical maximum limits of energy densities related to the heart beat or walking motion of 1 Hz would be 4 mW cm^{-3} for electromagnetic and electrostatic transduction, and 18 mW cm^{-3} for piezoelectric transduction [44, 69]. The picture is different in reality since the small nature of the harvesters exhibits resonance frequencies in the kHz domain which reduces the coupling to the external frequency source [78-80]. Although 1 mW cm^{-3} has been considered feasible, this will scale down with size resulting in a 1 mm^3 device generating a power that is 1000 times smaller. Although electrostatic energy harvesters could be used for implantable medical applications, the pre-bias parts such as batteries and electrets (charge storage materials) is impractical [81-82]. Batteries have limited lifetime as well as increasing the weight, volume and complexity of the device whereas the primary aim in this discussion is a power supply avoidance of batteries. The charge stored in the electret is also known to decay in time which will reduce the efficiency and power generating properties of the harvester accordingly [82].

1.2.3.3. Chemical energy generators (Micro bio fuel cells)

Chemical energy harvesters based on fuel cells have received renewed attention as alternative power supplies to replace the use of batteries. These devices are based on the use of organic fuels, such as methanol, glucose or lactose and may be equipped with inorganic (abiotic) or biological catalysts based on enzymes or whole organisms [72]. Fuel cells are electrochemical devices that is equipped with a cathode and an anode and which generate current through the oxidation and a reduction reaction of two chemical fuels (reactants) that is flowing into cell. Compared to batteries, micro bio-fuel cells are expected to operate for longer times due to the use of exogenous fuels that may not be depleted with time. For medical applications inside the body, glucose is the most promising candidate for the organic fuel used in the micro bio fuel cells. The concept of the µGFC is given in detail in chapter 2.

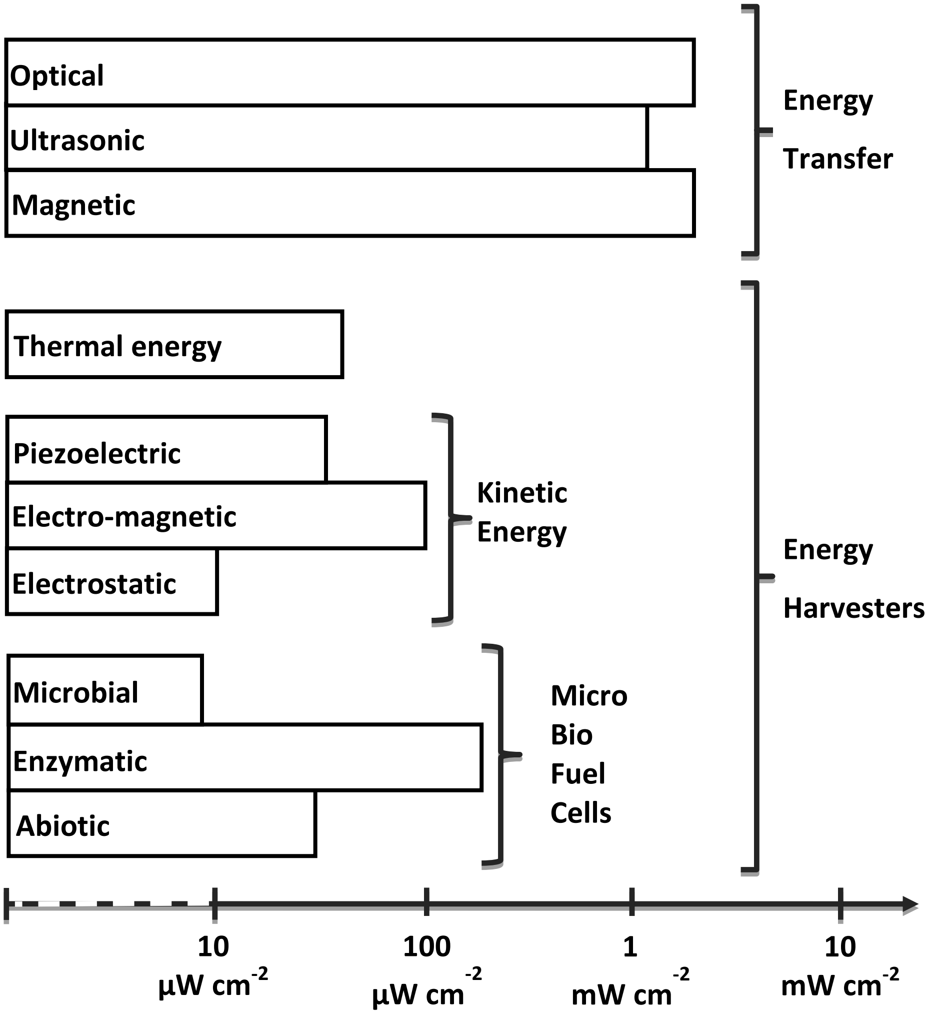

Figure 1-3: Comparable power densities of the different types of power supplies considered for use in implantable medical devices. [18, 49, 52, 80, 83-84]

2. Micro glucose fuel cells

2.1. Operation principle

Similar to conventional fuel cells, the electrochemical reactions of glucose and oxygen occur at two electrodes which are spatially separated by a separator membrane. A series of electrons, released from the electro-oxidation of glucose at the anode, flows through an external load circuit to the cathode where oxygen as the terminal electron acceptor is reduced. The driving force of the electron flow is the difference in the electrochemical potential of the two electrodes. In order to close the circuit and to keep the initial charge of the electrode constant, protons released from the oxidation process, will flow from the anode through the separator membrane and to the cathode if the reaction takes place in an acid electrolyte. In alkaline electrolytes, the flow will be subject to anions flowing in the opposite direction.

The chemical reaction of a glucose molecule ($C_6H_{12}O_6$) with oxygen (O_2) could theoretically give a perfect combustion and release 24 electrons per glucose molecule if permitted to go through all the series of chemical transformations until the generation of the end-products: carbon dioxide (CO_2) and water (H_2O). A summary of the reaction is given below with its standard Gibbs free energy (ΔG^o) and the standard potential (U^o) [20]

$$C_6H_{12}O_6 + 6O_2 \rightarrow 6CO_2 + 18H_2O \qquad \Delta G^o = -2.87 \times 10^6 \ (\text{J mol}^{-1}) \ [20]$$

$$U^o = 1.24 \text{ V} \ [20]$$

Considering the chemical reactions happening completely with an acid separator membranes or acid medium allowing the flow of proton (H^+), the reactions at the two electrodes could be given by [85]:

Anode: $C_6H_{12}O_6 + 6\ H_2O \rightarrow 6CO_2 + 24H^+ + 24e^-$

Cathode: $6O_2 + 24H^+ + 24e^- \rightarrow 12\ H_2O$

Considering reactions in an alkaline medium or separator membrane permitting the flow of anions (OH^-), the complete chemical reactions at the respective electrodes would be given by [85]:

Anode: $C_6H_{12}O_6 + 24OH^- \rightarrow 6CO_2 + 18H_2O + 24e^-$

Cathode: $6O_2 + 12H_2O + 24e^- \rightarrow 24OH^-$

A complete oxidation and the release of 24 electrons per glucose molecule is not a practical result in an artificial fuel cell system due to the lack of the reaction mediators. This is supported by the fact that CO_2 has not been found among the reaction products in any µGFC tests based on inorganic or enzymatic catalysts [85]. Gluconic acid, $C_6H_{12}O_7$, is usually reported as the main product of glucose oxidation in an acid, neutral and alkaline medium [20, 86-88]. It is the product of the first phase in the oxidation process of glucose [86]. The reaction to generate $C_6H_{12}O_7$ from $C_6H_{12}O_6$ releases only 2 electrons per glucose molecule [20, 85]. The overall reaction describing the cell behaviour, its ΔG^o and U^o could be given as:

$C_6H_{12}O_6 + ½\ O_2 \rightarrow C_6H_{12}O_7$ $\Delta G^o = -2.51 \times 10^5\ (J\ mol^{-1})$ [20]

$U^o = 1.30\ V$ [20]

The reactions of glucose oxidation and oxygen reduction in the acid and neutral medium or with the acid separator membranes could be given as [85]:

Anode: $C_6H_{12}O_6 + H_2O \rightarrow C_6H_{12}O_7 + 2H^+ + 2e^-$

Cathode: $½\ O_2 + 2H^+ + 2e^- \rightarrow H_2O$

When the µGFC use alkaline separator membranes or operate in a neutral or alkaline medium, the reactions at the electrodes could be [20, 85]:

Anode: $C_6H_{12}O_6 + 2OH^- \rightarrow C_6H_{12}O_7 + H_2O + 2e^-$

Cathode: $\frac{1}{2}O_2 + H_2O + 2e^- \rightarrow 2OH^-$

2.2. Classification of µGFC based on the catalysts

In general, µGFC can be categorized into three main types based on the nature of the catalyst used to facilitate the electrode reactions: (i) enzymatic, (ii) microbial and (iii) abiotic µGFC. Some key features of these different µGFC are summarized in Table 2-1.

Table 2-1: Key features of implantable µGFC

Type of µGFC	**Enzymatic**	**Microbial**	**Abiotic**
Catalysts	Isolated enzymes	- Whole, electro-active micro-organisms - The catalysts are located inside living cells like bacteria	- Noble metals and their alloys - Activated carbon
Demonstrated *in vitro* lifetime range [84]	Weeks	Years	Months
In vitro power density range (µW cm^{-2}) [84]	~ 250	~ 7	~ 4 - 50
In vivo power density range (µW cm^{-2}) [84]	~ 2.4 – 150	-	~ 2.2 - 40

2.2.1. Enzymatic µGFC

Enzymatic µGFC employ insulated enzymes such as glucose oxidase (GOx) or glucose dehydrogenase as the catalysts at the anode and laccase, bilirubin oxidase or copper oxidases as the catalysts at the cathode [89-91]. An example of the chemical reaction happening in an enzymatic µGFC is shown in Figure 2-1. The first enzyme-based biofuel cell using GOx as the anodic catalyst and glucose as the fuel was reported in

1964 by Yahiro as an attempt to create an alternative power supply for cardiac pacemakers [92]. With the development of the Li/I$_2$ batteries leaping the performance of glucose fuel cells at that time, further development lay dormant over several decades until 2001, when research on enzymatic µGFC were revived by Chen *et. al.* [92-93]. The highlights of the enzymatic µGFC development since 1964 are presented in Table 2-2.

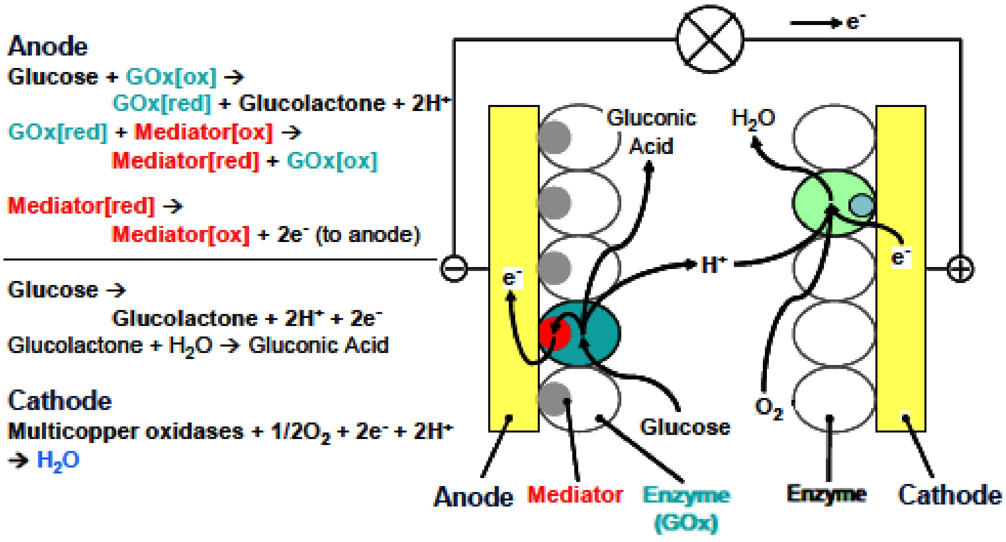
Anode
Glucose + GOx[ox] → GOx[red] + Glucolactone + 2H+
GOx[red] + Mediator[ox] → Mediator[red] + GOx[ox]
Mediator[red] → Mediator[ox] + 2e- (to anode)
Glucose → Glucolactone + 2H+ + 2e-
Glucolactone + H2O → Gluconic Acid
Cathode
Multicopper oxidases + 1/2O2 + 2e- + 2H+ → H2O
e-
Gluconic Acid
H2O
H+
e-
e-
O2
Glucose
Anode
Mediator
Enzyme (GOx)
Enzyme
Cathode

Figure 2-1: Example of chemical reaction with GOx as anodic catalyst, multicopper oxidases as cathodic catalyst and electron transfer mediator [94].

The utilization of enzymes as biocatalysts provides several benefits such as maintaining a high selectivity and thereby confining the correct reactions to the anode and cathode. This prevents the reactant from reacting at both electrodes at the same time and gives the possibility of a simple design without electrode compartmentalization which will facilitate miniaturization [85, 90]. The use of enzymes also provides defined reaction pathways on the electrode surface and overcomes the mass transfer resistances across the cell membranes in microbial µGFC [89]. However, they also have some drawbacks compared to other µGFC. Similar to microbial µGFC but in contrast to abiotic ones, electrical communication between the enzymes and the electrode surface is difficult to establish [95]. As shown in Figure 2-1, mediators are required to facilitate electron transfer from the enzyme to the electrode [94]. In addition, the progressive deactivation of enzymes due to the degradation of their complex protein structure over time limits the overall lifetime of the fuel cell [85, 96]. Compared to the microbial µGFC, enzymes are not able to compete with microbes in terms of fuel utilization, i.e. complete oxidation, and long-term stability [96].

Table 2-2: Highlights of the main achievements in the development of enzymatic μGFC.

Year [Ref.]	**Catalyst / Electrodes**	**Test condition**	**Performance**
1964 [92]	Glucose oxidase (anode) Pt (cathode)	-	
2001 [93]	Glucose oxidase (anode) Laccase (cathode) Osmium-containing polymers (electron transfer agents)	An aerated 15 mM glucose solution, pH 5.0	64 μW cm^{-2} (23°C) 138 μW cm^{-2} (37°C)
2002 [91]	Bilirubin oxidase (cathode) Glucose hydrogenase (anode) Osmium-based redox polymer (electron transfer agents)	PBS pH 7.0, 50 mM Glucose, 25^0C, O_2 saturated	58 μW cm^{-2}
2003 [97]	Glucose oxidase (anode) Bilirubin oxidase (cathode)	A living grape plant	430 μW cm^{-2}
2003 [98]	Bilirubin oxidase (cathode) Redox polymers	PBS pH 7.4, 15 mM glucose, 37.5^0C, air saturated	50 μW cm^{-2} 30 μW cm^{-2} (2 days)
2005 [99]	Polymer-containing vitamin K3 (electron transfer agents)	PBS pH 7.0, 10 mM glucose, 37°C, air saturated	14.5 μW cm^{-2} 4 μW cm^{-2} (2 weeks)
2010 [100]	Glucose oxidase and catalase (anode) Quinhydrone and polyphenol oxidase (cathode)	PBS pH 7.2, 5.5 mM glucose, room temperature, air saturated	1.47 μW (first 25 hours) 1.65 ± 0.13 μW (in the 30th – 40th day)
		In the retroperitoneal space of a male, freely moving Wistar rat	6.5 μW - 24.4 μW mL^{-1} 2 μW – 7.52 μW mL^{-1} (2.8 hours)

2.2.2. Microbial µGFC

Microbial µGFC utilize the enzymatic systems of whole, electro-active micro-organisms as the catalysts or the catalysts that are located inside living cells such as bacteria and human cell [20, 101]. The potential for using micro-organisms as biocatalysts was first realized through the work of Potter in 1912 [102] and later confirmed by Davis et. al. using fuel cells based on E.coli [103]. An example of chemical reactions occurring inside the microbial µGFC using S.Cerevisiae is shown in Figure 2-2. Highlights of the microbial µGFC development since 1964 are presented in Table 2-3.

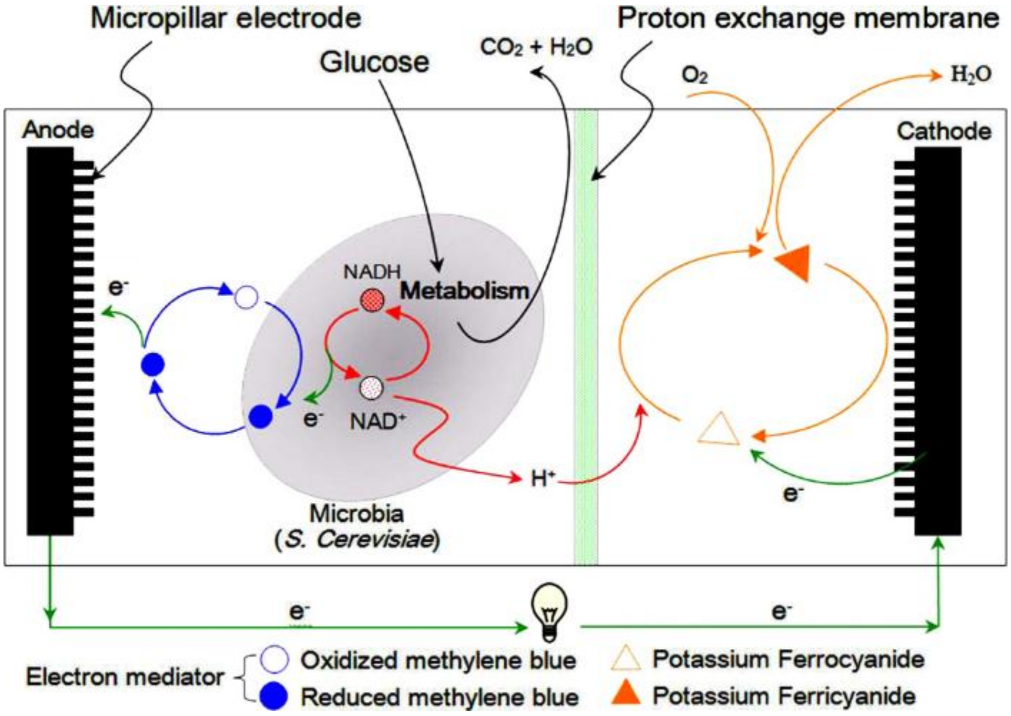
Micropillar electrode
Glucose
CO2 + H2O
Proton exchange membrane
O2
H2O
Anode
Cathode
NADH
Metabolism
e-
e-
NAD+
H+
e-
Microbia
(S. Cerevisiae)
e-
e-
Electron mediator
○ Oxidized methylene blue
● Reduced methylene blue
△ Potassium Ferrocyanide
▲ Potassium Ferricyanide

Figure 2-2: An example of the chemical reactions occurring inside a microbial µGFC using *S. Cerevisiae* [104]

Since microbial populations reproduce, the number of catalytically active elements should be continuously maintained, suggesting a longer lifetime for this kind of microbial µGFC [85]. However, the main disadvantage is an extreme difficulty in transferring the electrons produced by the reactions inside the cells to the electrodes.

This combined with a lower density of enzymes per unit area/volume leads to an overall poorer performance than the enzymatic µGFC [85]. Although the use of mediators, like nicotinamide adenine dinucleotide (NADH) as shown in Figure 2-2, is one possible solution, the compounds must satisfy some requirements, such as biocompatibility and the ability of electrons to be transported across the cell membranes of the micro-organisms [105]. Further, the health risks posed from the colonizing and infective nature of most microorganisms, suggests that current microbial µGFC should not be considered as an alternative power supply for implantable medical devices [20, 85].

Table 2-3: Highlights of the main achievements in microbial µGFC development

Year [Ref.]	**Catalyst**	**Test condition**	**Performance**
1912 [102]	Saccharomyces cerevisiae	0.55 M glucose culture medium (mixture of 50 g yeast and 100 c.c water)	0.32 V (open circuit potential)
1962 [103]	E. Coli (anode) Glucose oxidase (cathode)	Half cell, PBS pH 7.0, glucose present in glucose-oxidase systems only	1.764 µW
2005 [101]	Human white blood cells (anode); Potassium ferricyanide (cathode)	Human white blood cells (anode) PBS pH 7.4 (cathode)	0.729 nW cm^{-2}
2008 [104]	Saccharomyces cerevisiae (anode); Potassium ferricyanide (cathode)	Human plasma containing 4.2 mM blood glucose	42.4 nW cm^{-2} in 60 min
2010 [106]	Anaerobic micro-organisms (anode) Pt (cathode)	Simulated environment of transverse colon (37°C): Anode: simulated intestinal fluid (pH 7.8) with the inoculum from the fresh fecal samples, 0.14 mg L^{-1} oxygen Cathode: simulated intestinal fluid (pH 8.3) without fecal samples, 0.27 – 0.45 mg L^{-1} oxygen	7.33 µW cm^{-2} (maximum) 2 months (stable operation)
2013 [107]	Simulated colonic content (anode) Pt (cathode)	Simulated environment of transverse colon, pH 6.58	1.173 µW cm^{-2} (maximum) 100 hours (stable operation)

2.2.3. Abiotic µGFC

The third type of µGFC employs non-biological catalysts, normally named abiotic catalysts. These catalysts revolve around the use of noble metals (and their alloys) or activated carbon. Although the abiotic µGFC produce lower power density than the enzymatic and microorganism ones, they suggest various benefits over the others in terms of implantable applications. Thanks to the high melting temperature of most noble metals (and activated carbon) and the use of non-biological elements, they can be sterilized using standard sterilization protocols (such as steam sterilization at 121^{o}C) before operation [108-109]. Their inert surfaces and resistance towards oxidation gives long-term stability offering considerable durability by not depending on biological agents that degrade with time [85].

Although abiotic µGFC were firstly developed as an alternative power generator for medical implants (a demonstration of their feasibility to supply energy to cardiac pacemakers was shown *in vitro* as well as in animal trials in the late 1960s), the introduction of Li-based batteries in 1972 and the consequent enhancement of pacemaker battery lifetime resulted in very few subsequent reports on these fuel cells [20]. However, the attention on these fuel cell systems resumed with the works of Kerzenmacher in 2008 [20], and a more detail review on the state-of-art of abiotic µGFC for implantable medical applications is given in section 2.4, including their historical development, construction and performance.

2.3. Construction consideration and challenges of µGFC

Although implantable µGFC shares a similar working concept to external fuel cells, their operating parameters cannot be precisely controlled or optimized. The reactant concentrations, working temperature, reactant inflow rates and fluid composition are limited by the body physiology and on the location of the implant.

The pH of body fluids, for instance, is fixed and usually slightly alkaline, for example pH 7.35-7.45 for blood and pH 7.3-7.35 for cerebrospinal fluid [85]. The working temperature is considered similar to that of the body core temperature at 37^{o}C. The range of glucose concentration varies at different locations in the human body: 3.9-6.7 mM for blood plasma [110], 2.5-4.4 mM for cerebrospinal fluid [110] and 3.0-4.0 mM for interstitial fluid [20]. It is the same trend for oxygen concentration: 10-13.3 kPa (0.088-0.117 mM) for blood plasma [111], 3.3-6.6 kPa (0.029-0.058 mM) for cerebrospinal fluid [110], and 5.1-8.0 kPa (0.045-0.071 mM) for interstitial fluid [108]. Since the availability of glucose and oxygen is presented as a mixture in body fluids, the simultaneous occurrence of these reactants at both electrodes might result in an electrochemical short-circuit due to similar potentials created at both electrodes. Apart from the consideration of the size and shape (like for other implantable medical devices), the biocompatibility of the µGFC is an important aspect to be considered. This is because they cannot be completely hermetically sealed (as in pacemakers) but instead they have a window or an orifice that permits direct contact with the body fluids to maintain a continuous supply of reactants. All their components, therefore, should be fully biocompatible towards the body and at the same time be protected from detrimental effects caused by the same body fluids (biofouling). All these factors need to be controlled carefully in order to ensure long term stability that ultimately remain one of the most critical parameters of their future success. For example, if the µGFC were to supply energy for an implantable device of similar longevity as the artificial pacemaker, they would only succeed if they are able to operate *in vivo* for more than 10 years.

2.4. Implantable abiotically catalysed glucose fuel cells

2.4.1. Historical development

The potential of using abiotic catalysts started with the use of Pt electrodes for the anodic oxidation of cellulose and lower carbohydrates by Bockris in 1964 [112]. The first abiotic glucose fuel cell was introduced as a future power supply for implantable medical devices by Warner and Robinson in 1967 [113]. In 1968, a prototype, namely “Bioautofuel Cell” with two platinized electrodes in separate beakers, was reported by Wolfson [114]. In the following years, several reports on implantable abiotic µGFC were presented through academic and corporate activities, such as the catalyst material development of Monsanto Research Corporation, Union Carbide, German Robert Bosch GmbH and the US-based Leesona Moos Corporation [20]. The first truly abiotic µGFC for cardiac pacemaker applications were demonstrated by Drake *et al.* and Wolfson *et al.* in 1970 [115-116]. Due to the significant effect of the Li-based battery introduction in 1972, the research on the abiotic µGFC has not been very attractive until 2008 with the works of Kerzenmacher [20]. Some significant improvements of the abiotic µGFC are summarized in Table 2-4.

Table 2-4: Highlights of the main achievements in abiotical µGFC development since 1967

Year [Ref.]	**µGFC Catalyst / Design**	**Test conditions**	**Performance** (µW cm^{-2}, time)
1967 [113]	- Catalysed conducting electrodes (not clearly specified types of catalysts) - Cation exchange polymer membranes	- 10wt% (0.56 mol L^{-1}) glucose solution (unbuffered) & atmospheric oxygen	165 µW cm^{-2} first 24h, then a rapid decrease
1968 [114] Namely "Bio-auto-fuel cell"	- Platinized Pt electrodes immersed in two separated beakers	- 2 separate beakers (Cathode beaker – air; anode beaker – 5 mM glucose solution without oxygen) - Phosphate and bicarbonate buffer - Electrolyte pH not clearly specified	3.5 µW cm^{-2} in 18 days
1970 [115] Figure 2-3.a	- Bifacial access for anode / cathode. Cathode: Pt black laminated on one side of a hydrophobic carbon / PTFE matrix; Anode: a porous plaque of a noble metal alloy black compressed onto a Pt screen; Protective membrane for cathode: thin silicone rubber membrane Separator and protective membrane for anode: dialysis membrane of the supported ionic hydrogel film type.	Tyrode's solution, 0.005M glucose, pH 7.4, oxygen in the gas phase (pO2 = 80 mm.Hg), 30 – 38^{o}C	2.2 µW cm^{-2}, 144 hours 2.5 µW cm^{-2}, 428 hours 6.3 µW cm^{-2}, 167 hours
		- Implanted subcutaneously, right back flank of an adult mongrel female dog	2.2 µW cm^{-2}, 30 days
1970 [116]	- Two different porous platinized electrodes. - Separator membrane: Ion-exchange membrane	- Krebs-Ringer bicarbonate solution, pH 7.4, 5 mM glucose, 37^{o}C, oxygen pO_2 = 80-90 torr	24 µW cm^{-2}, 20 hours

1972 [117]	- Cathode: Teflon-bonded Pt black (15 mg Pt cm^{-2}) on a gold grid; Anode: Pt black 0.7% asbestos paste on gold grid (10 mg Pt cm^{-2}); Separator membrane: 178 µm anion exchange membrane	Implanted in a sheep vein	40 µW cm^{-2} initially, then quickly reduced within 1 hour
1976 [118]	- Cathode: activated carbon on metal screen - Anode: Pt-Ni Raney alloy catalyst. - Binders were not specified - Central anode was sandwiched between 2 cathodes - Epoxy frame	Subcutaneously in dog	4 µW cm^{-2}, 150 days
2006 [119] Figure 2-3.c (i)	- Depletion design with separator membrane to separate two electrodes; - Cathode: activated carbon; - Anode: activated carbon-based Pt-Bi alloy; - Separator: polypropylene filter	PBS pH 7.4, 0.1% glucose, air saturated, 37^{o}C	3.5 µW cm^{-2}
2007 [120]	- Cathode: Activated carbon - Anode: activated carbon with 5%Pt + 5%Bi - Separator: hydrogel membrane - Protective silicone rubber sheet	Aerated PBS pH 7.4, 0.1 wt% glucose, 37^{o}C	1.6 µW cm^{-2} after 2 days 1.1 µW cm^{-2} after 40 days
2008 [121] Figure 2-3.b	- Single layer fuel cell with two electrodes placed side by side - Cathode: Pt-Al - Anode: Pt-Zn	PBS pH 7.4, 7% oxygen saturation, 3 mM glucose, 37^{o}C	2 µW cm^{-2}

2008 [108]	- Cathode: Activated carbon - Anode: activated carbon with 5%Pt + 5%Bi - Separator membrane: polyethersulfone (Supor 450)	PBS pH 7.4, 5 mM glucose, 196 mbar oxygen, 37^{o}C	3.3 μW cm^{-2} after 10 days 1.0 μW cm^{-2} after 234 days
2012 [110] Figure 2-3.c (ii)	- Depletion design with separator membrane to separate two electrodes - Cathode: single-walled carbon nanotubes mesh embedded in Nafion - Anode: Pt-Al Raney alloy catalyst - Separator membrane: Nafion	PBS pH 7.4, 10 mM glucose, 18 - 24^{o}C Oxygen concentration: not specified	180 μW cm^{-2}
2013 [122]	- Cathode: Pt-Al Raney alloy catalyst - Anode: Pt-Ni Raney alloy catalyst - No separator membrane	- PBS pH 7.4, 5 mM glucose, 7% oxygen saturation, 37^{o}C	2 μW cm^{-2} after 12 hours
2014 [123]	- Cathode: Pt rod - Anode: ZnO – Au – Al - No separator membrane	- PBS pH 7.4, 5 mM glucose, air saturated, 22^{o}C	16.2 μW cm^{-2}

2.4.2. State of art of designs

In order to overcome the challenge of reactants being mixed together in the same medium, three main designs aiming for *in situ* separation between the oxidizing and reducing reagents have been proposed. All comes with both advantages and drawbacks.

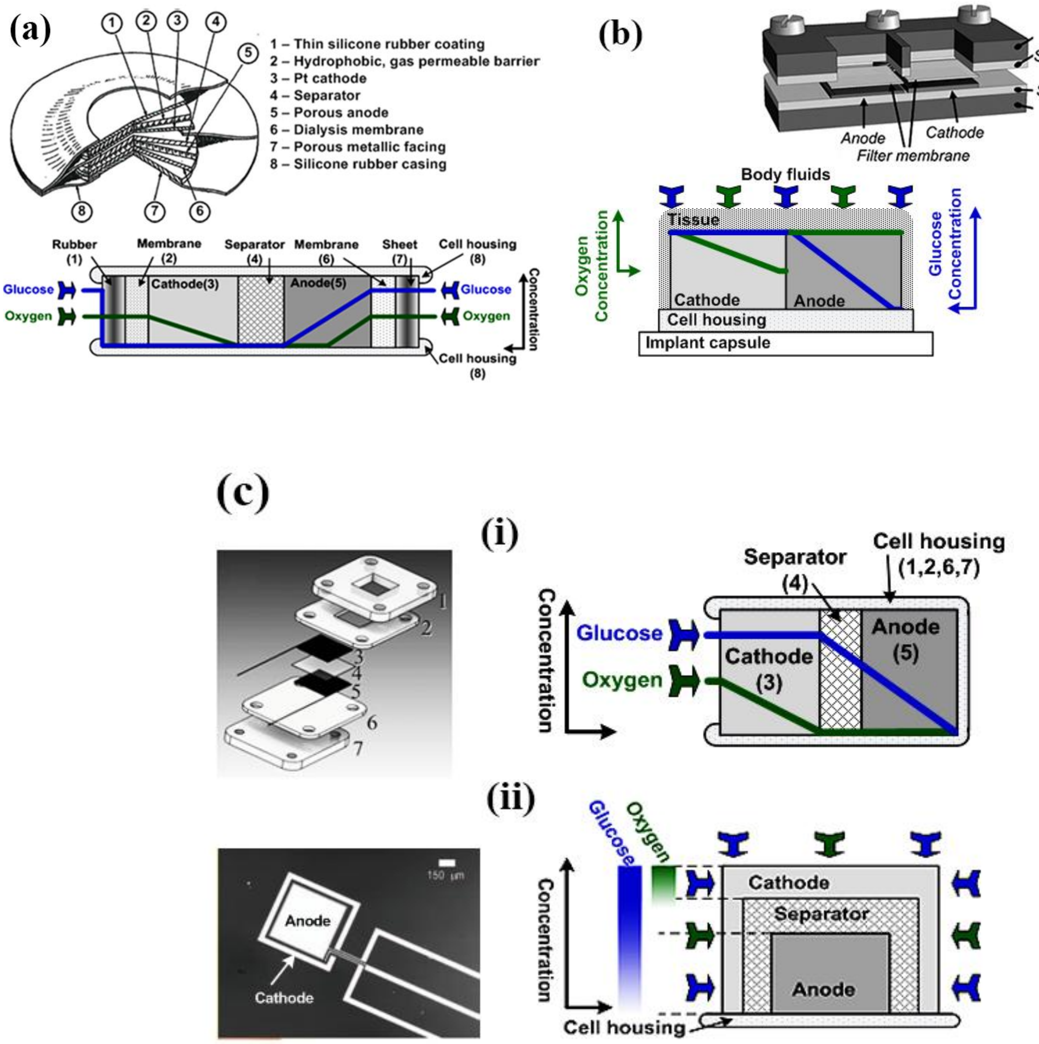
(a)
① ② ③ ④ ⑤
1 – Thin silicone rubber coating
2 – Hydrophobic, gas permeable barrier
3 – Pt cathode
4 – Separator
5 – Porous anode
6 – Dialysis membrane
7 – Porous metallic facing
8 – Silicone rubber casing
⑧ ⑦ ⑥
Rubber (1)
Membrane (2)
Separator (4)
Membrane (6)
Sheet (7)
Cell housing (8)
Cathode(3)
Anode(5)
Glucose
Oxygen
Glucose
Oxygen
Concentration
Cell housing (8)
(b)
PC
Silicone
Silicone
PC
Anode
Cathode
Filter membrane
Body fluids
Tissue
Oxygen Concentration
Glucose Concentration
Cathode
Anode
Cell housing
Implant capsule
(c)
1
2
3
4
5
6
7
(i)
Separator (4)
Cell housing (1,2,6,7)
Concentration
Glucose
Oxygen
Cathode (3)
Anode (5)
(ii)
150 µm
Anode
Cathode
Glucose
Oxygen
Concentration
Cathode
Separator
Anode
Cell housing

Figure 2-3: Three main designs of the abiotic µGFC intended for tissue implantation: (a) bifacial access to the anode and cathode [115] (b) single layer fuel cell with access from one face [121] (c) depletion (stacked) design using membranes to separate/reduce the flow of a specific reagent to the respective electrodes (i)[124] (ii)[110]

The first approach had separate openings for each electrode (bifacial access), and was introduced by Drake *et. al.* in 1970 [115]. As shown in Figure 2-3.a, a rapid consumption of all incoming oxygen, due to a direct reaction at the external surface of the anode, allows for a mixed potential to happen only in the outer regions of the "thick" anode layer [20, 108, 110-111]. The oxygen concentration consequently decreases significantly in the inner regions of the anode where glucose oxidation dominates. The Pt cathode located on the opposite side of the device is covered with a hydrophobic gas permeable membrane of polytetrafluoroethylene (PTFE) that blocks the access of glucose. Hence, one is able to achieve a reagent separation on one of the electrodes, and a partial separation on the second. In addition, there is no requirement of the reactant selective catalysts at both electrodes which is another advantage. This design makes use of the large difference in the physiological concentration between dissolved oxygen (DO) and glucose concentration in which the former is two orders of magnitude smaller than the latter (shown in section 2.3). The reactant separation is more effective at a low oxygen concentration which also decreases the cathode performance. Therefore, a trade-off between the reactant separation and the cathode performance is one of the drawbacks. This design was initially intended for use in blood stream and tissue implantation [20, 125].

The second approach designed as a "single-layer glucose fuel cell" was proposed by Kloke *et al.* in 2008 [121]. As shown in Figure 2-3.b, an equally sized cathode and anode were placed side by side at the same level and in direct contact with the solution containing a mixture of glucose and oxygen. Thus, the cathode and the anode must employ oxygen and glucose selective catalysts, respectively. Otherwise, mixed potential formation at both electrodes would cause a significant decrease in the cell potential and consequently reduce the performance of the devices. The requirement of excellent reactant selective catalysts at both electrodes which does not exist in real life is a drawback of this design. However, it has an advantage of the possibility to reduce the device volume because there is no need to stack the layers on top of each other and enables the potential of using it as a thin-layer coating on the external surface of implant capsules or pacemakers [85, 121].

The third approach was initially suggested by Rao *et al.* in 1974, named “depletion design” or stacked assembly, and is currently receiving the attention of many researchers [19]. As shown in Figure 2-3.c, the cathode uses oxygen-selective and glucose-insensitive catalysts mounted in front of the anode. The removal of oxygen at the cathode will help to create anoxic conditions at the anode and in this manner help to reduce the mixed potential formation at the anode due to the absence of dissolved oxygen. Although the large difference between the oxygen and the glucose concentrations in the physiological solution helps the solution to become mostly oxygen-free when reaching the anode, no pure oxygen-selective catalyst exists in real life which makes it difficult to remove all of the oxygen. The “depletion” abiotic µGFC could have single, double or multi-face inputs (Figure 2-3.c-i and Figure 2-3.c-ii). The reactants diffuse into the µGFC from an opening on one side in the single input arrangement as shown in Figure 2-3.c-i [88, 110, 126-127]. The two-sided input design allows two inlets of the reactant solution go through two cathodes at both sides of the package with the anode placed in between the cathodes [86]. In the multi-face input design in Figure 2-3.c-ii, the anode is placed on the substrate, surrounded by a three dimensional arrangement of the electrolyte / separator and porous cathode, paving way for a larger surface to volume ratio of the fuel cell device [110]. An advantage of this design is that it could simplify the implantation procedures by integrating the cell directly on the exterior surface of the pacemaker or on top of an impermeable implant capsule [20, 88, 110, 126-127].

2.4.3. State of art of construction

The following sections describe the main parts of an abiotic µGFC structure.

2.4.3.1. Electrodes with selective catalysts

In general, electrodes fabricated specially for an implantable abiotic µGFC can be divided into binder-based and binder-less types. Similar to the electrodes used in the conventional hydrogen fuel cells, binder-based electrodes are fabricated using a non-catalytic material (e.g. PTFE or polymer hydrogels) as an immobilizing body for the catalytic materials present as either a metal or graphite/carbon powder [115, 128-129]. In contrast, a continuous catalyst film or particles is deposited directly on a conducting substrate made from graphite sheets or metals in binder-less electrodes [115, 128-129]. A special kind of binder-less electrode explored in this thesis is fabricated from non-noble metals alloyed with Pt, namely Raney-Pt electrodes.

Among metal catalysts, Pt shows the best general performance towards both oxygen reduction and glucose oxidation if these reagents are loaded separately. However, it is not the best option if the solution contains both glucose and oxygen [114]. Other materials should instead be considered if you want to achieve a degree of selectivity towards oxygen, such as activated carbon [130], carbon nanotube [110] or pure metals such as palladium (Pd), gold (Au), silver (Ag) [130] or Raney-Pt alloys such as Pt-Al [122, 131] or Pt-Cu [126, 132-133]. There are also various selective materials for the catalysis of glucose such as Pt/Bi particles [108, 134], Rhodium (Rh), Iridium (Ir) [20, 135] and Raney-Pt alloys such as Pt-Cu, Pt-Ni, Pt-Zn and Pt-Al [110, 127, 136-137]. Some important selective catalysts are summarized in Table 2-4.

2.4.3.2. Separator membranes

Similar to conventional PEM fuel cells, the separator membranes in the µGFC work as ion conductors. Based on the ionic nature and corresponding capability to conduct ions, they can be divided into acidic membranes (also known as proton exchange membranes –PEM, or cation exchange membranes - CEM), and alkaline membranes (also known as anion exchange membranes - AEM). Acidic membranes (e.g. the brand name Nafion), permit the transport of protons (H^+) whereas alkaline membranes (e.g.

the brand name Fumasep, Sustainion) permit anionic (OH^-) flows [33, 138-140]. The ability to transport either proton or anion affects the reactions at the electrodes, as shown in section 2.1.

Unlike conventional PEM fuel cells, the ion conduction function of the separator membranes in µGFC can also be achieved by the buffer solution due to the short distances between the electrodes. In this case, the solution maintains electrical insulation between the two electrodes as well as permitting diffusion of the reactants, the products, and ions. Some kind of mechanical separation is still required to prevent the electrodes from coming into direct contact with each other. This can be achieved using membranes or mats from porous hydrophilic polyethersulfone (Supor 450), cellophane film, nonwoven mats of nylon fibers and even asbestos sheets [88, 115, 126, 133]. Such non electrolytic separator membranes are summarised in Table 2-4.

2.4.3.3. Protective membranes and cell housing

The external package of implantable abiotic µGFC should comply with the requirements posed for other implantable medical devices. It therefore must be compatible with the implantation site as well as the operational environment. Literature has so far revealed packaging options that renders this part as a preliminary phase, where the components are joined with adhesive tape, room temperature vulcanizing glue or cyanolit glue [115, 117, 141] and inserted into packages made from porous metal supports, epoxy or polycarbonate frames [88, 115, 127, 141-142].

In the package of the implantable abiotic µGFC, protective membranes function as the interface between the devices and tissue or blood in the body environment. They must have tissue and blood compatibility. They must be permeable to allow reactants and products go through. At the same time, they block larger molecules such as enzymes or proteins from coming into contact with the electrodes to prevent deactivation, degradation of the catalytic properties or even fouling the catalyst layer. Various membranes used as separators also could be employed as protective membranes, such as cellulose, cuprophane, dialysis tube, cation exchange hydrogels of poly(vinyl alcohol)-poly(acrylic acid), glycolmethancrylate type, and polyethersulfone [19, 86, 88, 141]. Silicone rubber or PTFE membranes have also been used as protective membranes to protect the cathodes from the interference of glucose and other endogenous substances [115-116].

3. Materials and Methods

3.1. Electrode fabrication

3.1.1. Nanoporous oxygen selective Pd cathodes

In short, the fabrication process of the nanoporous oxygen selective cathodes was achieved by depositing the catalyst film on top of porous substrates made from commercial aluminum oxide (AAO) membranes supplied from Fisher Scientific, UK. They have a diameter of 13 mm, a thickness of 60 µm and a pore size of 100 nm (Anodisc 6809-7013) or 200 nm (Anodisc 6809-7023). These were selected as the electrode substrates due to several favourable characteristics: Ceramic AAO are chemically inert as well as having good thermal stability [143-144]. They have a relatively high porosity that permits glucose, reactive by-products as well as components of the neutral physiological buffer solution to diffuse through. The pore size is uniform, thus reducing the danger of sectors with larger pores or defects, which may permit oxygen to diffuse through without being reduced and thereby interact with the underlying electrode (anode). They are also electrical insulating and can therefore be used as a spacer between the electrodes in the case of not using a specific separator membrane. Their large real surface area enhances both the area and consequently the catalytic activity of the catalyst film deposited on top.

The material of the catalyst for the oxygen reduction reaction was chosen very carefully in order to obtain the primary two requirements of being “sensitive” towards oxygen and “insensitive” towards glucose. Because Pt and Raney-Pt alloys present good catalytic activity for both oxygen reduction and glucose oxidation, they are not good candidates for the oxygen selective cathode [108, 121, 131]. Although activated carbon is a good option, it was found to have a lower catalytic activity than Raney-Pt alloy in the presence of glucose [120, 134]. Other catalysts such as ferric phthalocyanine, Au, Ag have weakness of poor catalytic properties towards oxygen reduction or being too sensitive towards glucose oxidation [108]. However, Pd has exhibited favourable properties towards oxygen reduction with respect to glucose oxidation in an isotonic saline solution at pH 7.22 [108]. It is also readily available in microfabrication labs. Hence, Pd was considered the best starting point investigating the catalytic properties of oxygen reduction in neutral physiological media (pH 7.4), in the presence of glucose.

A custom-made holder, shown in Figure 3-1, was used to hold up to 14 AAO membranes in one batch upside down without inducing stress during catalyst deposition of 100 to 200 nm Pd by e-beam evaporation. The holder was rotated at an angle during the deposition process to obtain better Pd coverage around the pore rim and inside the vertical walls of the pores. The fabrication process of the nanoporous oxygen selective cathode was presented in detail in Article I [25].

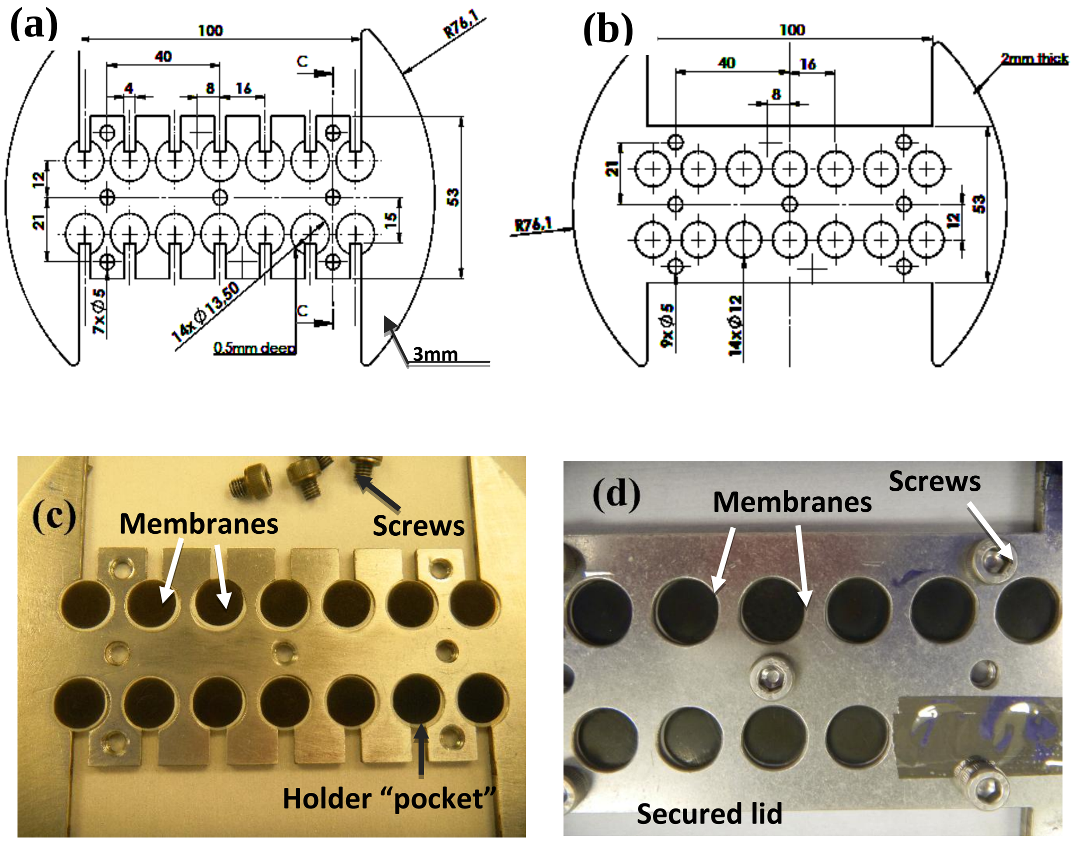
(a)
100
40
4
8
16
C
R76,1
12
21
53
15
7xØ5
14xØ13,50
0.5mm deep
3mm
(b)
100
40
16
8
2mm thick
21
R76,1
12
53
9xØ5
14xØ12
(c)
Membranes
Screws
Holder "pocket"
(d)
Membranes
Screws
Secured lid

Figure 3-1: The AAO membranes were held in place during the metal deposition process using a custom holder that permitted (a,c) positioning in "pockets" located in the base, on which a lid was attached (b,d) to prevent them from coming loose.

3.1.2. Raney Pt-Ni anodes

A literature survey was used to find the material suitable for glucose oxidation. As mentioned earlier, Pt may not be the best candidate for the anodic catalyst due to its universally good catalytic activity towards both oxygen and glucose as well as being prone to inactivation from glucose reaction intermediates with time. In contrast, Raney-Pt alloys, for example Pt-Zn, Pt-Pb, Pt-Ni or Pt-Al, are also promising candidates for abiotic catalysis due to their lower cost of production [23, 110, 127, 137]. Moreover, their characteristic with a preferred catalytic activity towards glucose with respect to oxygen is an important parameter considering use in implantable devices operating in a mixed fuel environment. It is also less prone to inactivation from glucose reaction intermediates. However, most Raney-Pt alloys have been synthesized from “thicker” electroplated films in the micrometer regime, and the performance of Pt-Ni thin films (< 1 μm) made by evaporation have not been investigated. Thus, this study aimed to see how a thin film of Raney-Pt (Pt-Ni) performed under simulated physiological conditions both in the presence and absence of oxygen.

The fabrication process of the Pt-Ni anode was presented in detail in Article III [26]. In short, three thin metal films of Ti, Pt and Ni, were deposited in order, by e-beam evaporation, onto single side polished Si wafers. After the wafers were diced into small samples, the samples were annealed at high temperatures in an inert environment. Chemical cleaning in a hot acid mixture removed unalloyed Ni and any Ni oxide formed due to the presence of residual oxygen in the annealing process. The anode samples were then prepared according to the protocol described in section 3.2.1 before being subjected to an electrochemical etching process that removed any remaining Ni and Ni oxide.

3.2. Sample preparation

3.2.1. Electrodes

The samples of the nanoporous oxygen selective cathode were used either in full or prepared by dicing into smaller pieces of approximately 5x5 mm^2. Samples of the Raney-Pt thin film anode were prepared by dicing the wafers into 5x5 mm^2 large samples with a dicing saw (DAD - 2H/6T, Disco Corp., Japan). They were then attached to a standard 1x3” glass slide by silicone rubber (3140 RTV Coating, Dow Corning, US). For analysis of the scanning electron microscopy (SEM) and energy dispersive X-Ray spectroscopy (EDS), a piece of copper tape was applied for electrical conduction from the electrode sample to the ground of the equipment in order to obtain good results. Copper wires were attached on top of the metal surface with the aid of silver epoxy (EPO-TEK EE129-4, Epoxy Technology, Inc., US). The copper wire bond was covered by additional silicone to insulate it from the aqueous testing solution so that only the catalyst surface was exposed to the solution. An example of a packaged electrode ready for use in subsequent electrochemical studies (surface area, catalytic performance and electrochemical impedance spectroscopy) is shown in Figure 3-2.

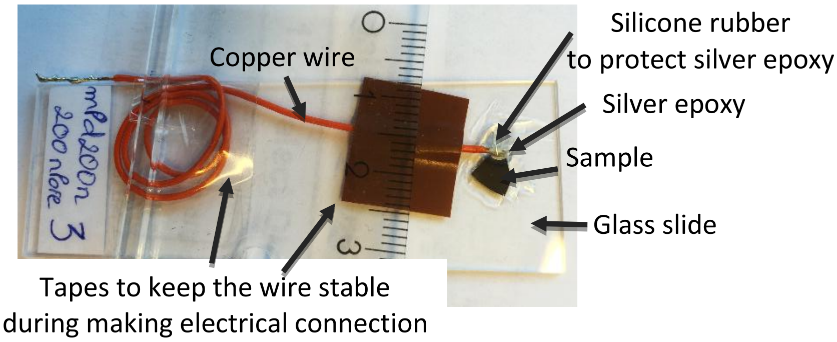

Figure 3-2: As prepared electrode ready for use.

3.2.2. Fuel cell

A stacked fuel cell assembly was realized, inspired by the “depletion design” proposed by Rao *et al.* [19], but with the difference of being made from thin film metal catalysts on both the cathodes and the anodes (Figure 3-3). The intention of this design was to ensure that when the reactants started to diffuse through the pores, most of the oxygen should be removed by the cathode before coming into contact with the anode. The transport of reactants occurs by diffusion because any methods of mechanical translocation will consume too much energy.

The stacked fuel cell assembly was designed in house. Inside a polyetheretherketone (PEEK) carrier, a 13 mm circular porous Pd cathode (section 3.1.1) was positioned with the catalyst film facing up on top of a 5x5 mm Pt-Ni anode (section 3.1.2) and a 5x5 mm large Nafion film stacked in between. The stacked electrode layer was immersed in phosphate buffered saline (PBS) containing both 5 mM glucose and 0.06 mM DO to simulate a real *in vivo* test condition. The electrical separation and ionic conduction between two electrodes were realized by the PBS filled channels of the porous AAO membrane and the Nafion film. An O-ring was used to separate the cathode from the protective metal frame at the top surface of the carrier. Silicone rubber sealed of the gap at the wall between the anode, the Nafion film and the cathode to ensure that the test solution could only access the anode throught the pores of the cathode. The work on the fuel cell assembly have been described in detail in Article IV [27].

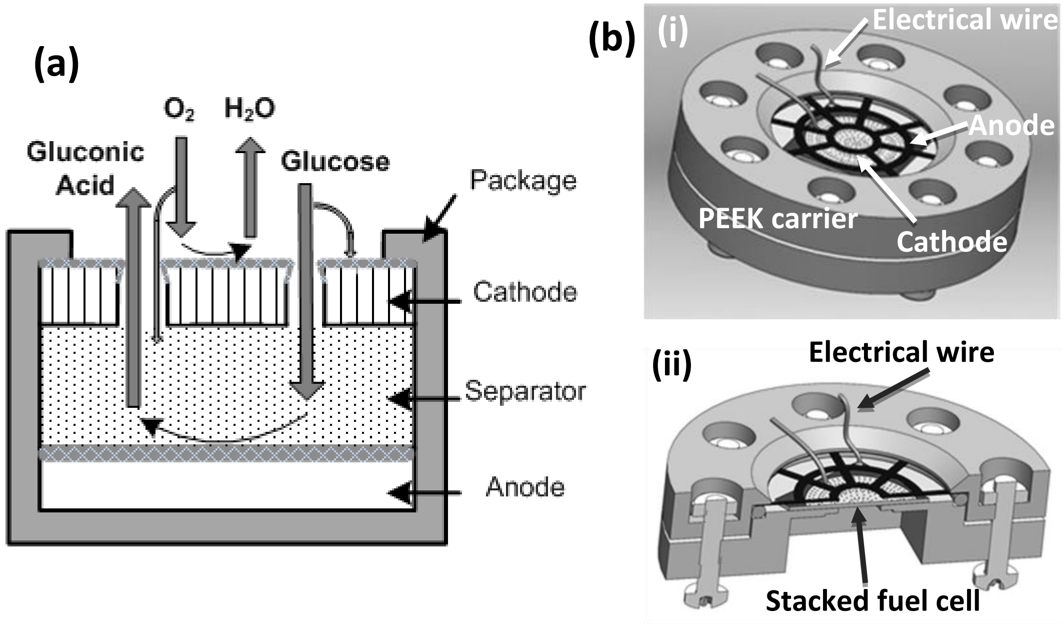
(a)
O_2
H_2O
Gluconic Acid
Glucose
Package
Cathode
Separator
Anode
(b)
(i)
Electrical wire
Anode
PEEK carrier
Cathode
(ii)
Electrical wire
Stacked fuel cell

Figure 3-3: (a) Schematic representation of the fuel cell assembly (b) stacked fuel cell assembly (i) whole piece (ii) cross section

3.3. Determination of the real surface area

3.3.1. Consideration of real area vs. geometrical area

Most real surfaces of the electrodes in the electrochemical experiments include micro- / nano-topographic structures and trenches that are not visible on the macroscopic scale. A substantial increase in the effective or real surface area of the electrodes would increase the number of chemically reactive sites and give the impression of a more active catalyst compared to a smoother surface of the same material. Therefore, the increase in the surface area ratio, which is the ratio between the real area (A_{real}) and the geometric surface area (A_{geo}) – sometimes referred to as roughness factor f_r =

A_{real} / A_{geo} in literature, would be an important property for electrodes with a small geometric area in order to enhance their catalytic performance. The measurement of the absolute or real surface area of a specific material is a field where mistakes are made if one fails to take into consideration the type of material and the nature of the surface topography investigated. Especially, gold (Au) and palladium (Pd), used to replace platinum (Pt), have their own properties that prevents the use of some common methods available for Pt. For example, standard hydrogen underpotential deposition is not suitable since the desired monolayer of adsorbed hydrogen needed for the area estimation does not form on the surface of the Au electrodes whereas Pd would adsorb hydrogen beyond the monolayer concentration [145-146]. The popular use of the Randles-Sevcik equation combined with the hexacyanoferrate (II/III), $[Fe(CN)_6]^{4-/3-}$ redox couples will neither work if the topographies are below the diffusion layer thickness. Consequently, an independent study on some selected methods which were available in our laboratories was presented in Article II on two selected materials, Pd and Au [30] – both proposed electrode materials for use in the cathode. The methods include two *ex situ* methods (SEM and AFM) and four *in situ* methods (the oxide formation and reduction from CVs, the double layer capacitance from the EIS measurements, the adsorption and stripping of iodine (I), and the use of the Randles-Sevcik equation / hexacyanoferrate (II/III), $[Fe(CN)_6]^{4-/3-}$ redox couple).

3.3.2. Nanoporous oxygen selective cathodes

The catalyst material for the nanoporous oxygen selective cathode used in this project (Pd) has some special and different properties that bring it apart from the universally applied catalyst material (Pt). One difference is that Pd absorbs hydrogen much more than its own volume. Thus, several popular methods, such as the hydrogen adsorption – desorption study used to estimate the active surface area of the Pt could not be used for the Pd electrode [29]. Neither the electrocatalysis of the Hexacyanoferrate (II/III), $[Fe(CN)_6]^{4-/3-}$, reductant-oxidant couple using the Randles–Sevcik equation [147] since the surface topography of thin films falls within the diffusion layer thickness which would mask away any net area increase below this magnitude. Instead, the oxide formation - reduction from cyclic voltammetry (CV) and double layer capacitance from EIS could be used to evaluate the active surface area of the Pd film [148]. The details of these processes for the area determination were presented in Article II [25]. In short, the real area of the cathode was found from the oxide formation – reduction method, which was determined by dividing the reduction charge of the Pd oxide (PdO) obtained from cyclic voltammograms (CVs) performed in sulfuric acid (H_2SO_4) solutions with the charge density associated with the reduction of one monolayer of PdO, 424 $\mu C\ cm^{-2}$ [148] . The real area of the cathode was confirmed by double-layer capacitance measurements. In this method, the double-layer capacitance at the electode-electrolyte interface obtained by EIS was divided with the double-layer capacitance of an ideally smooth Pd surface (24.5 $\mu C\ cm^{-2}$ [149]) to achieve the real area of the cathode.

3.3.3. Raney Pt-Ni anodes

The real surface area of the Raney Pt-Ni anodes was estimated by the hydrogen adsorption – desorption study, which is a popular method used for Pt electrodes. With an assumption that one hydrogen atom is adsorbed on each active surface site, the real surface area of the anodes was achieved by dividing the charge related to the hydrogen adsorption peaks received from CVs in the H_2SO_4 solutions with the charge density of a smooth polycrystalline Pt electrode, 210 $\mu C\ cm^{-2}$ [28-29]. A detailed process has been presented in Article III [26].

3.4. Performance

3.4.1. Electrodes

The performance of each electrode was characterized by recording their potential response from a constant current step for a given time period. The testing solution was made from 500 mL of 10 mM PBS (pH 7.4) mixed with different concentrations of oxygen and glucose according to the experimental protocol. To simulate the physiological levels of glucose and oxygen in the body fluid, glucose (G7525, Sigma-Aldric, US) was added to the PBS solution whereas the addition of DO was controlled by mixing corresponding amounts of air and nitrogen gas. In the experiment of the cathode performance, the DO concentration was selected from 0.03 mM ≅ 1 ppm ≅ 3.5%, equivalent to the oxygen tension in active respiratory tissue with the femoral muscle of the mouse, to 0.06 mM ≅ 2 ppm ≅ 7%, which is the value found in the subcutaneous tissue of the human arm [108]. The glucose concentration was chosen from 3 to 5 mM to simulate the variation in physiological levels of the interstitial fluid in human tissue, and which permitted the susceptibility of the cathode towards glucose catalysis to be investigated [20]. A similar approach was used for the anodes. Keeping the glucose concentration fixed at 3 or 5 mM, a range of DO concentration was chosen from 0 to 7 ppm corresponding to the best and worst conditions, respectively. In the former all oxygen is removed at the cathode surface whereas the latter corresponds to the oxygen level found in air saturated solutions that is even higher than that found in the human body. The experimental processes for the electrode performance were presented in detail in Article I [25] for the cathode and Article III [26] for the anode.

3.4.2. Fuel cell

Two experimental setups were explored: a standard U-tube vessel, shown in Figure 3-4, and a stacked fuel cell assembly, shown in Figure 3-3.b. In the U-tube assembly, two electrodes were mounted in two separate compartments, as a proof-of-concept study to simulate the “best” and “worst” case scenario. Glucose and DO were added as separate reactants into the PBS solution in the respective compartment simulating the “best” case whereas a mixture of both glucose and DO was added in both compartments simulating the “worst” case. The results from the U-tube experiments were compared to the experiments using the stacked fuel cell assembly (described in section 3.2.2). The stacked assembly were immersed in a PBS solution containing both glucose and dissolve oxygen to simulate a real *in vivo* test condition. A detailed analysis is presented in Article IV.

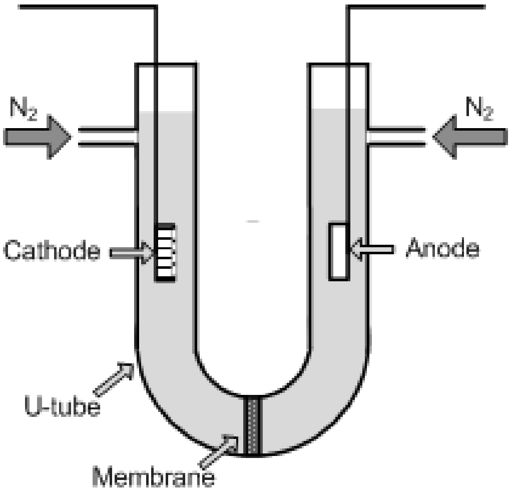

Figure 3-4: Experiment set-up with a U-tube cell. The shaded area corresponds to PBS buffer acting as both electrolyte and media for glucose and DO storage.

3.5. Electrochemical impedance spectroscopy (EIS)

The EIS analysis of the electrodes was performed using the EIS function of a Zahner electrochemical workstation (IM6, Zahner-elektrik GmbH, Germany) running in a galvanostatic mode. The samples in the EIS measurements were immersed in a 500 mL solution of 10 mM PBS (pH 7.4) at 25^{o}C. The simulation function of the electrochemical workstation was used to estimate the parameters of the components in electrical equivalent circuits. The circuit models for every electrode, shown in Figure 3-5, were considered to be applicable to a similar reaction scheme in the PBS solutions. Detailed protocols were presented in Article I [25] and Article III [26].

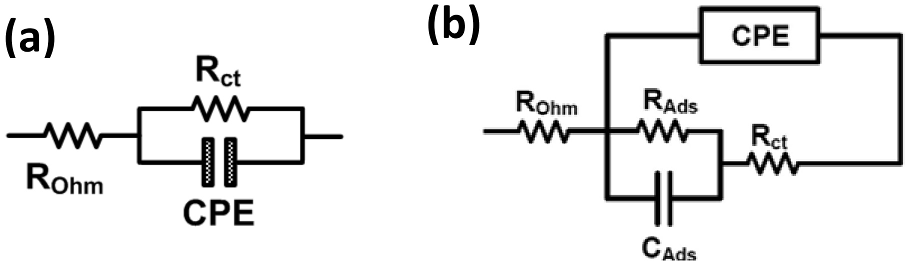
(a)
R_{ct}
R_{Ohm}
CPE
(b)
CPE
R_{Ohm}
R_{Ads}
R_{ct}
C_{Ads}

Figure 3-5: Circuit models used to fit the EIS analysis for electrodes (a) cathode (b) anode.

4. Results and discussion (summary of articles)

4.1. Determination of the real surface area

4.1.1. The Real Area of Nanoporous Catalytic Surfaces of Gold and Palladium in Aqueous Solutions (Article II) [30]

Among some methods presented here, the lowest values of the surface area ratio were obtained from the 2D SEM method because area contributions in the vertical direction were not considered. The 2D SEM method is only efficient to estimate the porosity level (holes vs solid surface) on the electrode surface and the surface area ratio obtained from this method is synonymous with porosity.

Another *ex situ* method available in this project, AFM characterization, was used to get the missing information in the vertical direction by providing a full assessment of the surface topography of the sample. However, one of the most critical challenges with the AFM method is the occurrence of artefacts due to the tip-sample convolution effect. The fraudulent features generated by the artefacts modify the real surface topography and affect the reliability of any dimensional information [150]. The quality of the AFM images having high aspect ratio features relies on the inclination of the working cantilever as well as the sharpness and geometry of the tips [151]. The surface area ratio estimated by AFM will therefore most likely be lower than its true value.

In contrast to the *ex situ* methods, like SEM and AFM, the *in situ* methods or the electro-chemical methods need an electrical conducting layer on top of the samples. The utilization of charge accumulation on the surface suggests the ability to penetrate any available crack, hole or crevice at the molecular scale.

Among four *in situ* methods mentioned here, the hexacyanoferrate (II/III) electrocatalysis (FE) based on the redox couple $[Fe(CN)_6]^{3-/4-}$ gave the lowest surface ratio. In this study, the linear relationship between the peak currents and the square root of the scan rate shows that mass transfer to the electrode surface is controlled by a one dimensional (1D) linear diffusion. If the surface topography is smaller than the diffusion layer, these topographic structures will be masked away within the diffusion layer which results in no consideration of the area contribution from these. The surface area will therefore be smaller than the real one. Moreover, the size of the samples used in this experiment was smaller than that suggested for the methods based on 1D diffusion limited transport [152]. Another diffusion mediated transport, namely radial diffusion, would also promote the diffusional transport of the redox couple at the electrode edges which causes a larger current and obvious larger surface area than that from the 1D model. However, the real surface areas estimated from this hexacyanoferrate (II/III) electrocatalysis are still affected by the masking of the surface topography caused by the combination of two diffusion mediated transport.

The no effect of the diffusion mediated transport on the iodine adsorption as well as the atomic scale of the iodine ion allows iodine to bond to any available area of the electrode and consequently those areas, even nm scale topographies, should be considered in this study. Therefore, the surface area ratio of the Pd and Au electrodes obtained from this iodine adsorption measurement (IA) is similar to the one estimated from the oxide formation and the double layer capacitance methods. However, the area determination of the Pd electrodes based on the iodine adsorption measurements should be used with caution because of the special property of the Pd material. The stripping of the disordered top-most Pd layers during the anodic process (peak 1 in the forward scan of CVs shown in Figure 4-1.a) just before the desorption of the adsorbed iodine I_{ads} was found to cause a smoothening of the Pd surface [153]. This smoother and more “planar” surface resulted in a decrease in the charges calculated from the main oxide reduction peaks (peak 2 in the potential region of 0.2 – 0.7 V shown in Figure 4-1.a). All of the Pd atoms on the electrode surface could be stripped and even the Pd samples could be destroyed if multiple CVs are used. In contrast to the Pd electrodes, the total charges Q_{tot} of the Au electrodes contained the charges from the oxidation of adsorbed iodine and the oxidation of Au whereas the background charge Q_{bg} was the charges from the oxidation of Au. The charges associated with the Au oxidation of the untreated electrodes have the same value as the charges obtained from the oxide reduction of the iodine pretreated electrodes, peak 2 in Figure 4-1.b, (Q_{bg}). After calculating the charges from the iodine oxidation process Q_{iod} by subtracting Q_{bg} from Q_{tot}, the real surface area of the Au electrodes was estimated by using equation [4] in article II [30].

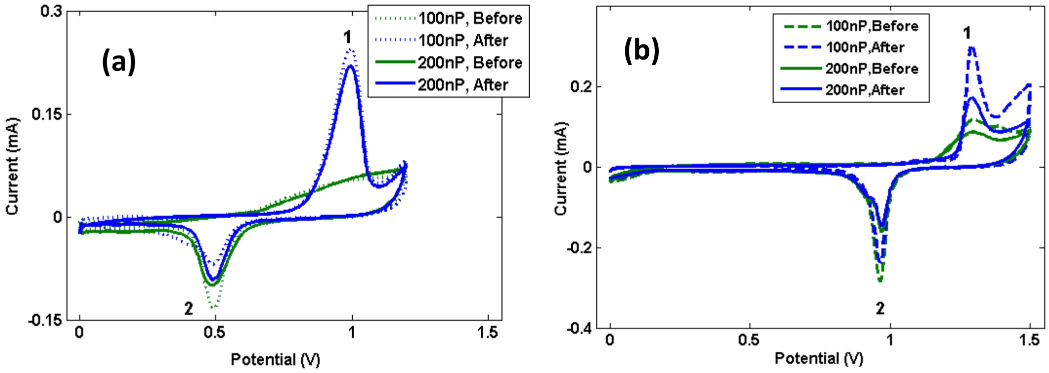

Figure 4-1: CVs showing the oxidation of iodine-adsorbed to (a) Pd and (b) Au electrodes with 100 and 200 nm pores.

Although the surface area ratio estimated from the oxide formation measurements (OF) in Figure 4-2 gave the largest values among those methods used here, this method is considered to be less reliable than that based on hydrogen adsorption due to the reduction of the reliability with the increase in the affinity of the metals toward oxygen. Furthermore, the charge densities as well as the potential range involved with the reduction or the formation of one oxide monolayer play an important role. Because those values were calculated theoretically or studied under different experimental conditions, they should be selected very carefully [29, 146, 148, 154-156]. For the Au electrodes, the uncertainty in the determination of the Burshtein minimum current also affects the potential range for one monolayer formation [157]. The selected charge densities as well as the potential range used in this study were based on the fact of similar experimental conditions taken from literature [148, 154-155, 158-159].

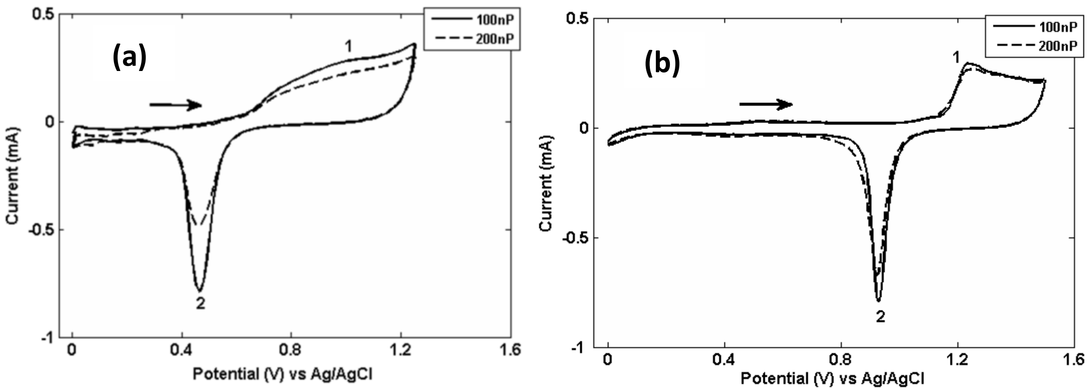

Figure 4-2: CVs of the (a) Pd electrodes and (b) Au electrodes with 100 and 200 nm pores. The arrow shows the scan direction.

Similar to the oxide formation measurements, the surface areas obtained from the double-layer capacitance (DLC) are affected by the experimental conditions as well as the reference double-layer capacitance values [149, 155-156]. The experimental results of the Pd electrodes fit well to the equivalent circuit in the inset (i) of Figure 4-3. The equivalent circuit for fitting the data of the Au electrodes could be changed into the circuit shown in inset (iii) of Figure 4-3 because the charge- transfer resistance R_c could be neglected due to their much larger values than that of the Ohmic resistance R_o (about 23 x 10^6 times). However, the same equivalent circuit in inset (iii) of Figure 4-3 was used for both the Pd and Au electrodes to compare their double layer capacitance C_{dl}.

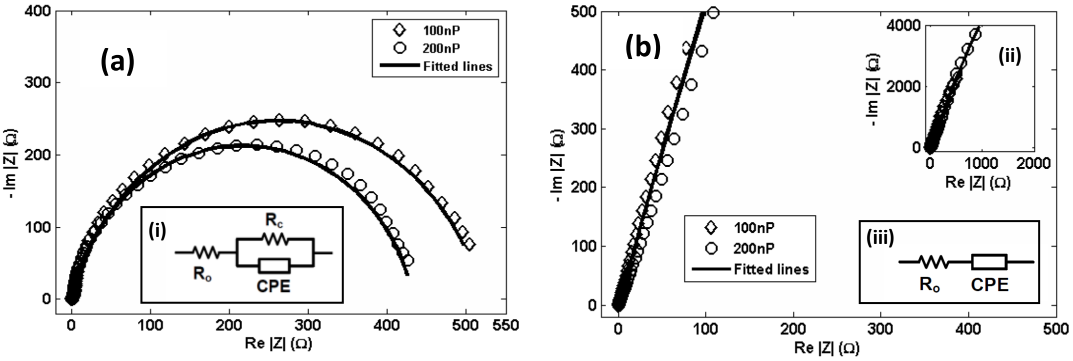

Figure 4-3: EIS curves of (a) the Pd electrodes and (b) the Au electrodes. The equivalent circuit for fitting the data of both electrodes is shown in inset (i). The full extension of the EIS curves from the Au electrodes is shown in inset (ii) is. The alternative equivalent circuit for fitting the data of the Au electrodes is shown in inset (iii).

These results are summarized in Figure 4-4. Among those methods, the similarity between the double-layer capacitance and the oxide formation measurement offers that these values would be the most correct representation of the real surface area for the Pd and Au electrodes investigated in this article.

Candidate's contribution: Original idea, design of setup, all experimental work, and main author.

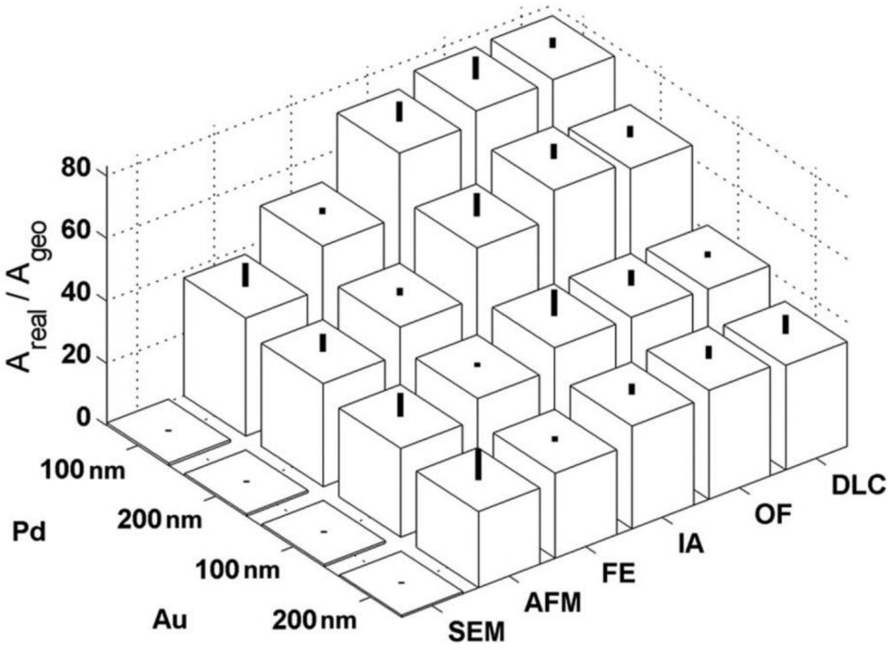

Figure 4-4: Comparative analysis of the different methods used to determine the real surface area. The black bar on the center top surface of the columns represents the standard error of the mean (n = 3 number of measurements).

4.1.2. Nanoporous oxygen selective Pd cathodes (Article I)

The real surface areas of the two Pd cathodes were estimated from the oxide reduction measurement (9.5 ± 0.6 and 7.8 ± 0.9 cm^2 for the Pd cathodes with 100 and 200 nm pore sizes, respectively). These are comparable with the ones obtained from the double-layer capacitance measurement, (10 ± 0.6 and 8.4 ± 0.5 cm^2 for the Pd cathodes with 100 and 200 pore sizes, respectively). With the geometric area of the Pd cathodes (0.097 ± 0.03 and 0.101 ± 0.05 cm^2 for the Pd cathode with the pore size of 100 and 200 nm, respectively), the roughness factors $f_r = \frac{A_{real}}{A_{geo}}$ were found to be 103 ± 0.3 and 83 ± 0.4 for the Pd cathodes with the pore size of 100 and 200 nm, respectively. It shows that the Pd cathodes with 100 nm pores have a larger real surface area than cathodes with 200 nm pores, possible due to a lower overall porosity of the AAO substrates.

Candidate's contribution: Original idea, design of setup, all experimental work, and main author.

4.1.3. Raney Pt-Ni anodes (Article III)

Based on the charge recorded from the hydrogen adsorption peaks the real surface areas A_{real} of 38 ± 7 and 80 ± 5 cm^2 for the anodes annealed at 650°C and 800°C, respectively, were found to be 235 ± 44 and 492 ± 32 times larger than the geometrical surface area, A_{geo}, respectively. This suggests that a higher annealing temperature promotes the migration of Ni and Pt, resulting in larger regions of alloy that remains intact. The electrochemical removal of Ni resulted in deeper trenches or “creavasses” causing an enlargement of the surface area. Although these values are smaller than that reported by Gebhardt et al. [28] for electrodes made from thicker layers of Pt and Ni (150 µm Ni on top of a 100 µm thick Pt foil) annealed at 1450°C, it is clear that the surface topography of the electrode scales with the thickness of the material used.

Candidate’s contribution: Original idea, design of setup, all experimental work, and main author.

4.2. Performance

4.2.1. Thin film nanoporous electrodes for the selective catalysis of oxygen in abiotically catalysed micro glucose fuel cells (Article I)

This article presents the development of nanoporous electrodes for oxygen reduction in the presence of glucose, and which were later used as the cathode in the fuel cell assembly. The fabrication was carried out during a summer intern placement at the University of California at Berkeley under the supervision of Prof. Michele Maharbiz. The samples were then brought home for subsequent characterization in the labs of USN. The results from the experimental approach of tilting a rotating sample with respect to the deposition source were partial successful in that it permitted Pd to be deposited inside the rim of the pore. However, the clustered appearance revealed that this material had most likely no direct electrical connection to the uniform layer at the top surface, and would thus not contribute in the oxygen removal process (Figure 4-5).

The metal catalyst deposition also provided means of reducing the pore size if required. The exchange current density was found from a simple Butler-Volmer analysis (Tafel slope of - 60 mV dec^{-1}) extracted from the polarization curves. This paper also introduced the concept of effective exchange current density based on the intrinsic exchange current density and the contribution from the real surface area represented by the roughness factor f_r (section 4.1.2). Thus, the measured exchange current density of 2.9 x 10^{-3} ± 0.5 x 10^{-3} μA cm^{-2} for the Pd electrodes would in fact be the effective exchange current density with the real (intrinsic) current density being a factor smaller scaled with the f_r. The electrode potential was also recorded with respect to the concentration of DO and glucose concluding with longevity tests showing a reduction in the electrode operational potential of only -0.13 mV h^{-1} under a load current density of 4.4 μA cm^{-2}. This reduction in the electrode potential could come from the adsorption of glucose and reaction intermediates which gradually deactivates the catalytic surface. It also could result from the degradation of the electrical contact which was made by attaching copper wires directly on the top metal surface of the porous AAO membrane with silver epoxy and covered by silicone. The potential reduction would affect the long-term performance of the electrodes if there is no improvement in the electrical contact as well as in the removing of adsorbed substances covering the catalyst surface which is one avenue of future work to be explored as a result of this project. The area specific resistance (ASR) ranged from 224.8 ± 13.2 to 249.9 ± 4.1 Ω cm^2 with the Pd electrodes with the largest surface area (AAO substrates with 100 nm pores) having the lowest resistance. This result is in contrast to classical macro fuel cell electrodes based on, for example, carbon cloth [38] where the electrolyte resistance dominates.

Considering the electrode potential under load, comparable literature values show that these are approx. 50 mV higher [131]. The reason could come from the morphology of the electrode surface and the adsorption of glucose on the electrode surface. The Pd-based electrodes with a roughness factor between 83 to 103 are not as rough as the electrodes found in literature with a roughness factor between 135 to 149, and which results in potentially fewer active reaction sites [131]. This will reduce the positive electrode potential under comparable current loads. The number of reaction sites could also reduce more if the glucose adsorption on the electrode surface is higher on the Pd electrodes made in this project. The adsorption properties of glucose change along with the morphology of the electrodes, where the adsorption increases more on smooth, plane electrode surfaces compared to rough surfaces [160].

With respect to the question if the Pd catalyst is truly selective towards oxygen reduction, or just resistant (less sensitive) to mixed potentials in the presence of glucose, so is it clear that the electrode potential was reduced when 5 mM glucose was added.

With the presence of 5 mM glucose, the observed reduction of electrode potential could be caused by adsorption of glucose as neutral molecules at the active electrode surface which decreases the number of reaction sites. The glucose sensitivity of the Pd-based cathodes under load and at open circuit is rather low compared to literature [131]. In the presence of both oxygen and glucose, the negative potential created by the glucose oxidation will reduce the electrode potential compared to that created by the oxygen reduction in the PBS without glucose present. This shows evidence of a mixed potential formation. The higher selectivity towards oxygen reduction and the lower selectivity towards glucose oxidation shown by the Pd catalyst reduces the mixed potential formation in the presence of glucose. Hence the underlying mechanisms could either be the adsorption of glucose at the active surface of the electrodes (blocking active sites), the higher selectivity towards oxygen reduction and the lower selectivity towards glucose oxidation of Pd (mixed potentials).

Candidate’s contribution: Original idea, design of experimental setup, all experimental work, and main author.

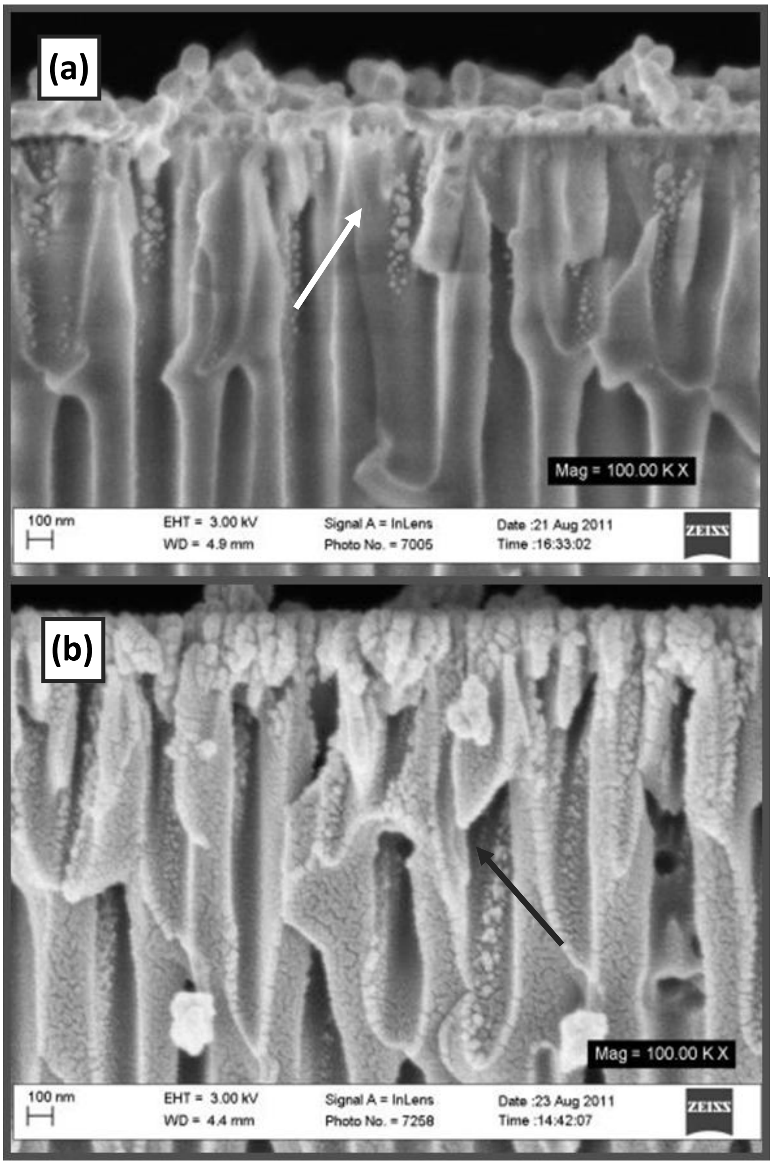
(a)
Mag = 100.00 K X
100 nm
EHT = 3.00 kV
WD = 4.9 mm
Signal A = InLens
Photo No. = 7005
Date :21 Aug 2011
Time :16:33:02
ZEISS
(b)
Mag = 100.00 K X
100 nm
EHT = 3.00 kV
WD = 4.4 mm
Signal A = InLens
Photo No. = 7258
Date :23 Aug 2011
Time :14:42:07
ZEISS

Figure 4-5: Deposition of metal clusters inside the pore rim of the AAO membrane substrate (arrows) with 200 nm pore size for (a) 100 nm thick Ag and (b) 200 nm thick Pd. The Ag was used as a test material before choosing Au and later Pd as the catalyst.

4.2.2. Raney-platinum thin film electrodes for the catalysis of glucose in abiotically catalysed micro-glucose fuel cells (Article III)

This article presents the development of a thin film platinum (Pt) and nickel (Ni) alloy designed as an anode for glucose catalysis in the fuel cell assembly at the neutral pH. These alloys, also known as Raney-platinum alloys, have previously been made using thicker electroplated films in contrast to evaporated thin films that were explored in this project. Thin films are defined as those with a thickness of 1 μm or below [24] which will limit the potential of creating 3D structures (and thus a corresponding increase in the real surface area) compared to those deposited using electroplated or screen printed thick film technologies. The rationale behind using thin film technologies, beyond that of being adopted from and thereby compatible with standard CMOS processing methodologies, is a net reduction in usage of the expensive metal used. The combination of high temperature annealing and electrochemical etching in the hot H_2SO_4 solution resulted in a grainy appearance that increased the surface area by almost 500 times (section 4.1.3) compared to the geometrical surface area (Figure 4-6). A direct calculation of the exchange current density from a simplified Butler-Volmer analysis was not possible since the catalysis from glucose to the expected product (gluconic acid) would be a multiple electron transfer process. Instead, the individual Tafel slopes were identified (249 - 266 mV dec^{-1}) and compared to the open circuit potential of the electrode annealed at 800°C. This enabled a relative comparison between the two electrodes to be made related to the surface roughness even though the exact exchange current density could not be found (the j_0 of the electrode annealed at 800°C being twice that of the electrode annealed at 650°C). Running under an extended testing regime for 72 hours in the presence of 5 mM glucose dissolved in air saturated PBS at a load current density of 2 $\mu A\ cm^{-2}$ revealed an increase in the electrode potential of only 23 $\mu V\ h^{-1}$. The ASR ranged from only $3.9 \pm 0.8\ \Omega\ cm^2$ (for the electrode annealed at 800°C) to $4.1 \pm 0.7\ \Omega\ cm^2$ (for the electrode annealed at 650°C). This was considerably lower than that recorded for the nanoporous cathodes (~225-250 Ω cm^2). These results suggest that the nanoporous Pt–Ni alloy anodes offer an improved catalytic stability with time and should be a viable candidate for use in abiotic catalysed glucose fuel cell systems operating under physiological conditions.

The more negative potential of the Pt-Zn electrodes compared to the Pt-Ni could come from the higher roughness factor of the Pt-Zn electrodes (1889 ± 155 and 2668 ± 179 [137]) compared to that of the Pt-Ni electrodes (235 ± 44 and 492 ± 32 [26]). The lower roughness factor or the lower real surface area of the Pt-Ni electrodes reduces the number of reaction sites which will reduce the negative potential generated. The main reason comes from the thinner catalyst film used in Pt-Ni electrodes (100 nm Pt film, 300 nm Ni) compared to the Pt-Zn electrodes (50 µm Pt, 30 µm Zn, [137]).

It was also found that the stabilities of Pt-Ni electrodes developed in this study and the Pt-Zn electrodes taken from literature [27] were similar under load (considering an experimental period of 80 hours). The degradation rates of the Pt-Zn electrodes were measured over a longer time period and thus appeared as being larger.

Candidate's contribution: Original idea, design of experimental setup, all experimental work, and main author.

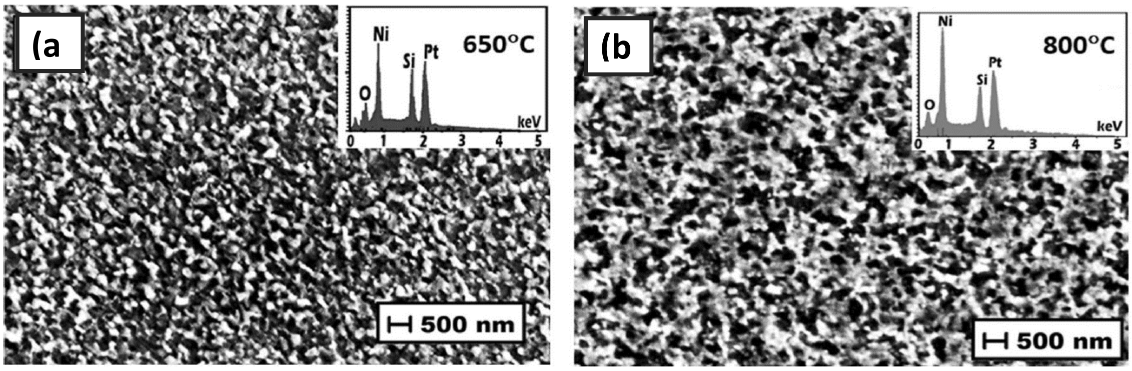

Figure 4-6: Surface architecture of the thin film Raney-Platinum alloy after fabrication annealed at (a) 650°C and (b) 800°C. The inserts show the EDS for the respective electrode surfaces.

4.2.3. A micro fuel cell for abiotical catalysis of glucose (Article IV)

This study presents the combination and assembly of the two electrode systems developed in Article I and Article III into a complete fuel cell device. In addition, a simulation study was performed seeking to relate the current densities with respect to the reagent flux and concentration as a function of pore size and catalyst thickness of the cathode. A dummy setup was made from a U-tube assembly in which the two electrodes were immersed in separate compartments connected through a porous glass frit. The use of separate compartments enabled control of the electrolyte composition and concentration of the individual reactants. In an ideal setting, the separation of the reactants could be simulated removing any tendency of the electrode to react with the wrong fuel, whereas a worst-case scenario would simulate the *in vivo* body conditions in which the reactants were fully mixed at both compartments. Any net current output here would be due to the catalytic differences of the two electrodes handling glucose catalysis and the oxygen reduction reaction, and if any cross reactions occur, the net power output would be smaller than in the idealized case. Finally, a stacked version of the fuel cell was made and compared to the conditions created in the U-tube experiment. If all the oxygen were consumed at the cathodic interface, and that the transport of glucose was similar to the ideal U-tube experiment, the power output should have been similar, and if the attempt to separate the reagents failed the power output would have been the same as for the worst case of U-tube experiment. As it happened, the power output was somewhere in between (Figure 4-7) with the cell being able to maintain 2.33 ± 0.11 µW cm^{-2} at a current density of 7.7 µA cm^{-2} and a cell potential of 0.30 ± 0.01 V. This was 80% of the power obtained in the ideal experiment.

This demonstrates the proof-of-concept of using a porous cathode with a Pd catalyst at the top surface to remove (part of) the DO and at the same time permitting a flux of glucose to the anode surface. The results were also favourable compared to the half-cell potentials and polarization curves taken from Article I and Article III respectively.

These differences could be attributed to changes in the electrode arrangement (omitting the counter and reference electrodes in the fuel cell assembly) as well as the implementation of a cleaning protocol using CV scans that would remove any surface oxide prior to the measurements.

Candidate's contribution: Original idea, design of experimental setup, all experimental work, simulation, and main author.

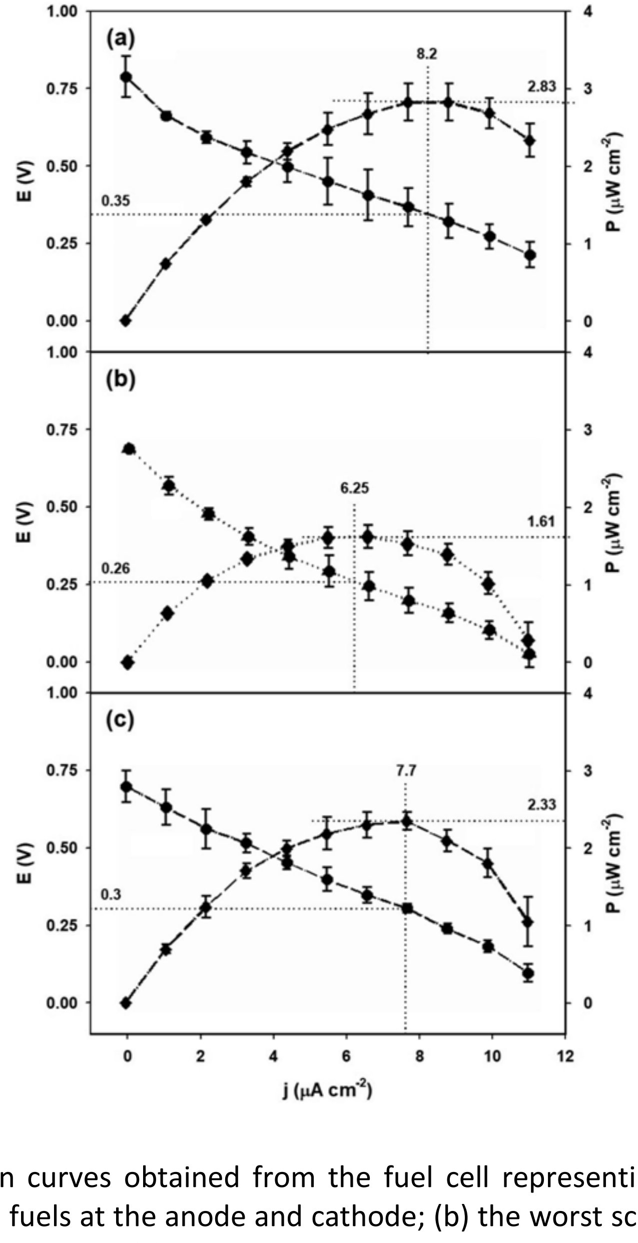

Figure 4-7: Polarization curves obtained from the fuel cell representing (a) the best scenario with separate fuels at the anode and cathode; (b) the worst scenario in which both reagents are mixed, and (c) using a stacked fuel cell assembly attempting a separation of the fuels in a mixed fuel environment. The error bars correspond to ± 1 std dev, n = 3 number of measurements.

5. Conclusion and future work

5.1. Conclusion

Energy harvesting within the body may provide the solution for powering long term medical implants, especially considering abiotical μGFC which utilize the same energy supply as the living cells, tissue and organs in which the implant resides. Thus, investing time and effort into developing such chemical harvesters would be beneficial if implantable micro devices become mainstreams with the large economic and societal impact that will follow.

This work details the development of a μGFC in which the design and materials were selected from the intended purpose of use as an implantable device in a mixed fuel environment. The results shows that one can make a porous cathode from a thin film Pd catalyst if this is combined with a porous substrate offering a rough surface facilitating an increase in the effective surface area reminiscent of a much thicker (screen printed or electroplated) catalyst layer. In this manner the use of expensive catalyst is reduced at the same time as the process can be tailored a microfabrication schedule with massive parallel processing resulting in a reduced cost per unit. However, the results are restricted to the narrow pore range explored (100 and 200 nm base diameter), as well as the anode being the limiting catalytic factor in the design resulting in oxygen escaping through the outer barrier created by the cathode and into the electrolyte separating the anode below. Also, the μGFC design relied on the conduction of protons through the pores of the Pd catalyst which would increase the internal resistance of the cell limiting the peak current generated.

The results also show that thin film Pt-Ni anodes could be generated with a reasonable catalytic activity by increasing its effective surface area. The benefit from the alloying process was exploited by removing unalloyed Ni with selective etching leaving the alloyed metal behind. Since the diffusion of Ni into Pt is not uniform following grain boundaries at different coefficients, the result was a 3D structure that enhanced the surface area by close to 500 times.

As originally intended, a question was raised if a stacked design of the chosen electrodes and electrolyte system would yield the desired benefits from reagent separation. Combining the electrodes into a µGFC provided the possibility to test that hypothesis. In order to do this, a reference test setup consisting of a standard U-cell with a porous glass frit enabling two separate compartments to be in ionic contact, was created. The U-cell was intended to test the performance from the electrode system subject to both separate and a mixed fuel environment. By comparing the stacked design with the reference tests, it was shown that a separation of glucose and oxygen from the mixture was achievable (at least partially). This acted as a proof-of-concept study showing that a stacked design with a nanoporous oxygen selective cathode, containing Pd catalyst films at the top surface, was able to generate a power density of 2.33 ± 0.11 µW cm^{-2}. This was found to be 1.45 times higher than that of the cell with separated electrodes operating in a mixed fuel environment and close to 80% of the cell working with separate reactants.

The determination of the real surface area plays an important role in quantifying parameters related to the electrochemical properties of the catalytic surface. During characterizing the electrochemical properties of the Pd cathodes, we realised that there were no universal methods available to estimate the real surface area in literature, especially for the Pd and Au electrodes. This was in spite of several available experimental methods, used mostly for Pt. Therefore, a spin off project arose to determine which experimental methods that were available in our lab (as well as most other micro-fab labs) would be suitable for assessing Pd and Au electrodes. We started off with some popularly known surface characterization methods and evolved into a comparative study between chosen *ex situ* and *in situ* models. The *ex situ* methods of using SEM and AFM, are universally applicable to most solid surfaces, both conducting and non-conducting. They provide structural information about the surface architecture and geometry, but only to the point of resolution of the instrumentation used. The SEM is not good in determining the 3D topography, whereas the resolution of the AFM in the lateral dimension is limited to the tip radius and structure of the needle. The *in situ* methods or electrochemical measurements require electrically conducting surfaces. Both iodine adsorption and electrocatalysis of the Hexacyanoferrate (II/III) redox couple gave larger surface area ratios than the *ex situ* methods. The iodine was shown to remodel the surface and hence topography, whereas the Hexacyanoferrate (II/III) redox couple were limited to diffusional transport of reactants – masking away any topographies below the thickness of this diffusion layer. The largest values were achieved from the oxide formation and the double layer capacitance measurement, which corroborated nicely against each other confirming that these two methods yield similar results and thus may be the most accurate. The choice of chemistries is also important as some materials may react with the surface (form irreversible bond, absorption) and hence mask away the value (e.g. current, charge, potential) obtained as a function of the surface area. This is an area in which the choice of method may be obvious for the chemist, but maybe not for scientists working in the different field of microfabrication, and from which miniaturized electrochemical instrumentation is developed. Hopefully this study was able clarify this message.

5.2. Future work

A special challenge of the µGFC will be to predict its long term *in vivo* performance based on the short term lab based *in vitro* evaluations. Simulating *in vivo* conditions, *in vitro* can be done by making a blood like solution in which the µGFC resides by mixing the physiological buffer used in this project with albumin and amino acids that may absorb on to the surface of the fuel cell (potentially blocking catalytic sites). This can be extended to blood plasma studies that include coagulation factors, as well as whole blood with cells etc (potentially blocking the porous cathode). These interfering species may significantly affect the performance, the stability as well as the longevity of the µGFC. It has been shown that anodes working under load in an artificial tissue fluid experience a quick positive shift of the anode potential [137] which a subsequent reduction in the cell potential generated. Therefore, a protective membrane should be used as an external barrier between the devices and the biological fluids of the body. A protective membrane with a special design in the mesh size or charge could block interfering molecules from coming into contact with the electrodes and thereby prevent deactivation or degradation of the catalysts (biofouling). The protective membranes should be biocompatible as well as permeable to permit reactants and products to pass through. Several materials such as alginate, cellulose, cuprophane, dialysis tube, cation exchange hydrogels of poly(vinyl alcohol)-poly(acrylic acid), glycolmethancrylate, polyethersulfone, silicone rubber or PTFE membranes could be viable candidates as a protective membrane [19, 86, 88, 141] [115-116]. Hence future studies should be taken to develop and implement a protective membrane covering the porous cathode based on the results achieved *in vitro*.

Future work will also focus on the optimization of long-term stability (from the current values -0.13 mV h^{-1} for the cathode and +23 μV h^{-1} for the anode) as well as reducing the internal electrical resistance by exploring a method in which the porous cathodes will be facing down towards the separator membranes inside the cells. This may reduce the flux rate of DO, but will be a compromise worth exploring as long as the anodes represent the limiting factor of the generated current density. Mass-transfer limitations can be enhanced by increasing the porosity of the cathodes and the active area available for substrate diffusion, but at the same time restricting the pore diameter at the catalyst interphase to prevent DO escaping into the separator cavity and down to the anode surface. Once confident, the operating ability of the glucose fuel cell should be explored in an endogenous environment inside the body by focusing on the biocompatibility and the effect of the tissue restructuring with time around the fuel cell implant.

An enhancement of the real surface area of the anode may also be attempted through the use of carbon nanotubes (CNT's), silicon grass, or other ways of modifying a planar substrate to a 3D structure prior to the deposition of the catalyst. In this manner, one may enhance the catalytic properties of the anode to better match that of the cathode.

References

1. ResearchAndMarkets. *$143.3 Billion Implantable Medical Devices Market - Global Industry Trends, Share, Size, Growth, Opportunity and Forecast 2019-2024*. 07/2019 [cited 12/2019; Available from: https://www.prnewswire.com/news-releases/143-3-billion-implantable-medical-devices-market---global-industry-trends-share-size-growth-opportunity-and-forecast-2019-2024--300879427.html.
2. FiorMarkets. *Global Active Implantable Medical Devices Market by Product (Ventricular Assist Devices, Neurostimulators, Others), End User, Region, Global Industry Analysis, Market Size, Share, Growth, Trends, and Forecast 2018 to 2025*. 01/2019 [cited 12/2019; Available from: https://www.fiormarkets.com/report/global-active-implantable-medical-devices-market-by-product-362199.html.
3. Zoll, P.M., *Resuscitation of the heart in ventricular standstill by external electric stimulation.* The New England Journal of Medicine, 1952. **247**: p. 768-771.
4. van Hemel, N.M. and E.E. van der Wall, *8 October 1958, D Day for the implantable pacemaker.* Netherlands Heart Journal, 2008. **16**(Suppl 1): p. S3-S4.
5. Bhatia, N. and M. El-Chami, *Leadless pacemakers: a contemporary review.* Journal of geriatric cardiology : JGC, 2018. **15**(4): p. 249-253.
6. Mallela, V.S., V. Ilankumaran, and N. Rao, *Trends in Cardiac Pacemaker Batteries.* Indian Pacing and Electrophysiology Journal, 2004. **4**(4): p. 201-212.
7. Martins, M.B.B., et al., *Cochlear implants: our experience and literature review.* International archives of otorhinolaryngology, 2012. **16**(4): p. 476-481.
8. Chuang, A.T., C.E. Margo, and P.B. Greenberg, *Retinal implants: a systematic review.* British Journal of Ophthalmology, 2014. **98**(7): p. 852.
9. Mulpuru, S.K., et al., *Cardiac Pacemakers: Function, Troubleshooting, and Management: Part 1 of a 2-Part Series.* Journal of the American College of Cardiology, 2017. **69**(2): p. 189-210.
10. Pashneh-Tala, S., S. MacNeil, and F. Claeyssens, *The Tissue-Engineered Vascular Graft-Past, Present, and Future.* Tissue engineering. Part B, Reviews, 2015. **22**(1): p. 68-100.
11. Cook, J.A., et al., *The total artificial heart.* Journal of thoracic disease, 2015. **7**(12): p. 2172-2180.
12. Verrills, P., C. Sinclair, and A. Barnard, *A review of spinal cord stimulation systems for chronic pain.* Journal of pain research, 2016. **9**: p. 481-492.
13. McAdams, B.H. and A.A. Rizvi, *An Overview of Insulin Pumps and Glucose Sensors for the Generalist.* Journal of clinical medicine, 2016. **5**(1): p. 5.
14. Westerman, S.B. and M. El-Chami, *The subcutaneous implantable cardioverter defibrillator--review of the recent data.* Journal of geriatric cardiology : JGC, 2018. **15**(3): p. 222-228.

15. Chakrabarty, B., A.K. Ghoshal, and M.K. Purkait, *Preparation, characterization and performance studies of polysulfone membranes using PVP as an additive.* Journal of Membrane Science, 2008. **315**(1-2): p. 36-47.
16. Wei, X. and J. Liu, *Power sources and electrical recharging strategies for implantable medical devices.* Frontiers of Energy and Power Engineering in China, 2008. **2**(1): p. 1-13.
17. Victoria, G., et al., *Bone stimulation for fracture healing: What's all the fuss?* Indian journal of orthopaedics, 2009. **43**(2): p. 117-120.
18. Ben Amar, A., A.B. Kouki, and H. Cao, *Power Approaches for Implantable Medical Devices.* Sensors (Basel, Switzerland), 2015. **15**(11): p. 28889-28914.
19. Rao, J.R. and G. Richter, *Implantable bio-electrochemical power sources.* Die Naturwissenschaften, 1974. **61**(5): p. 200-206.
20. Kerzenmacher, S., et al., *Energy harvesting by implantable abiotically catalyzed glucose fuel cells.* Journal of Power Sources, 2008. **182**: p. 1-17.
21. Savadogo, O., et al., *New palladium alloys catalyst for the oxygen reduction reaction in an acid medium.* Electrochemistry Communications, 2004. **6**(2): p. 105-109.
22. Sun, W., A. Hsu, and R. Chen, *Palladium-coated manganese dioxide catalysts for oxygen reduction reaction in alkaline media.* Journal of Power Sources, 2011. **196**(10): p. 4491-4498.
23. Gebhardt, U., J.R. Rao, and G.J. Richter, *A special type of raney-alloy catalyst used in compact biofuel cells.* Journal of Applied Electrochemistry, 1976. **6**(2): p. 127-134.
24. Harsha, K.S.S., *Principles of Vapor Deposition of Thin Films*. 2006: Elsevier Science.
25. Do, U.P., et al., *Thin film nanoporous electrodes for the selective catalysis of oxygen in abiotically catalysed micro glucose fuel cells.* Journal of Materials Science, 2016. **51**(19): p. 9095-9107.
26. Do, U.P., et al., *Raney-platinum thin film electrodes for the catalysis of glucose in abiotically catalyzed micro-glucose fuel cells.* Journal of Materials Science, 2019. **54**(22): p. 14143-14156.
27. Do, U.P., F. Seland, and E.A. Johannessen, *A micro fuel cell for abiotical catalysis of glucose.* Journal of Power Sources, 2020. **478**: p. 229032.
28. Łukaszewski, M., M. Soszko, and A. Czerwiński, *Electrochemical Methods of Real Surface Area Determination of Noble Metal Electrodes – an Overview.* International Journal of electrochemical science 2016. **11**: p. 4442-4469.
29. Trasatti, S. and O.A. Petrii, *Real surface area measurements in electrochemistry.* Journal of Electroanalytical Chemistry, 1992. **327**(1): p. 353-376.
30. Do, U.P., F. Seland, and E.A. Johannessen, *The Real Area of Nanoporous Catalytic Surfaces of Gold and Palladium in Aqueous Solutions.* Journal of The Electrochemical Society, 2018. **165**(5): p. H219-H228.
31. Bazaka, K. and M.V. Jacob, *Implantable Devices: Issues and Challenges.* Electronics, 2013. **2**(1): p. 1-34.

32. Joung, Y.-H., *Development of Implantable Medical Devices: From an Engineering Perspective.* International Neurourology Journal, 2013. **17**(3): p. 98-106.
33. Holmes, C.F., *The role of lithium batteries in modern health care.* Journal of Power Sources, 2001. **97-98**: p. 739-741.
34. Kim, D.-H., et al., *Epidermal Electronics.* Science, 2011. **333**(6044): p. 838.
35. Cao, H., et al., *Stretchable Electrochemical Impedance Sensors for Intravascular Detection of Lipid-Rich Lesions in New Zealand White Rabbits.* Biosensors & Bioelectronics, 2014. **54**: p. 610-616.
36. Johnson, C.S., *Development and utility of manganese oxides as cathodes in lithium batteries.* Journal of Power Sources, 2007. **165**(2): p. 559-565.
37. Greatbatch, W., et al., *Lithium/carbon monofluoride (Li/CFx): a new pacemaker battery.* Pacing and Clinical Electrophysiology: PACE, 1996. **19**: p. 1836-840.
38. Amatucci, G.G. and N. Pereira, *Fluoride based electrode materials for advanced energy storage devices.* Journal of Fluorine Chemistry, 2007. **128**(4): p. 243-262.
39. Takeuchi, E.S. and P. Piliero, *Lithium/silver vanadium oxide batteries with various silver to vanadium ratios.* Journal of Power Sources, 1987. **21**(2): p. 133-141.
40. Crespi, A., et al., *Modeling and Characterization of the Resistance of Lithium/SVO Batteries for Implantable Cardioverter Defibrillators.* Journal of The Electrochemical Society, 2001. **148**(1): p. A30-A37.
41. Bock, D.C., et al., *Batteries used to power implantable biomedical devices.* Electrochimica Acta, 2012. **84**: p. 155-164.
42. Drews, J., et al., *Primary batteries for implantable pacemakers and defibrillators.* Journal of Power Sources, 2001. **97-98**: p. 747-749.
43. Chen, K., et al., *Hybrid cathode lithium batteries for implantable medical applications.* Journal of Power Sources, 2006. **162**(2): p. 837-840.
44. Hannan, M.A., et al., *Energy harvesting for the implantable biomedical devices: issues and challenges.* BioMedical Engineering OnLine, 2014. **13**(1): p. 79.
45. Schroeppel, E.A., *Pacing lead with piezoelectric power generating means*, U. Patent, Editor. 1987, Cordis Corp: US US4690143A.
46. Pankratov, D., et al., *Ex vivo electric power generation in human blood using an enzymatic fuel cell in a vein replica.* RSC Advances, 2016. **6**(74): p. 70215-70220.
47. Murakawa, K., et al., *A wireless near-infrared energy system for medical implants.* IEEE Engineering in Medicine and Biology Magazine, 1999. **18**(6): p. 70-72.
48. Parkhouse, L., *Photovoltaic powered charging apparatus for implanted rechargeable batteries*, in *US Grant*, U. Grant, Editor. 2006, Quallion LLC US.
49. Goto, K., et al., *An implantable power supply with an optically rechargeable lithium battery.* IEEE Transactions on Biomedical Engineering, 2001. **48**(7): p. 830-833.
50. Song, K., et al., *Subdermal Flexible Solar Cell Arrays for Powering Medical Electronic Implants.* Advanced Healthcare Materials, 2016. **5**(13): p. 1572-1580.

51. Banerji, S., et al. *CMUT ultrasonic power link front-end for wireless power transfer deep in body*. in *2013 IEEE MTT-S International Microwave Workshop Series on RF and Wireless Technologies for Biomedical and Healthcare Applications (IMWS-BIO)*. 2013.
52. Cochran, G.V.B., M.P. Kadaba, and V.R. Palmieri, *External ultrasound can generate microampere direct currents in vivo from implanted piezoelectric materials.* Journal of Orthpaedic Research, 1988. **6**(1): p. 145-147.
53. O'Brien, W.D., Jr., *Ultrasound-biophysics mechanisms.* Progress in biophysics and molecular biology, 2007. **93**(1-3): p. 212-255.
54. Harrison, R.R., et al., *Wireless neural signal acquisition with single low-power integrated circuit.* Proceedings - IEEE International Symposium on Circuits and Systems, 2008: p. 1748--1751.
55. Makin, I.R.S., et al., *In-vivo demonstration of a self-contained ultrasound-based battery charging approach for medical implants.* The Journal of the Acoustical Society of America, 2017. **141**(5): p. 3956-3956.
56. Kennedy, J.E., G.R.t. Haar, and D. Cranston, *High intensity focused ultrasound: surgery of the future?* The British Journal of Radiology, 2003. **76**(909): p. 590-599.
57. Tesla, N., *Apparatus for transmitting electrical energy.*, in *US Grant*, U. Grant, Editor. 1914, Nikola Tesla US.
58. Sauer, C., et al. *Power harvesting and telemetry in CMOS for implanted devices*. in *IEEE International Workshop on Biomedical Circuits and Systems, 2004.* 2004.
59. Parramon, J., et al. *ASIC-based batteryless implantable telemetry microsystem for recording purposes*. in *Engineering in Medicine and Biology Society, 1997. Proceedings of the 19th Annual International Conference of the IEEE*. 1997.
60. Catrysse, M., B. Hermans, and R. Puers, *An inductive power system with integrated bi-directional data-transmission.* Sensors and Actuators A: Physical, 2004. **115**(2): p. 221-229.
61. Lenaerts, B. and R. Puers, *An inductive power link for a wireless endoscope.* Biosensors and Bioelectronics, 2007. **22**(7): p. 1390-1395.
62. Cao, H., et al., *An Implantable, Batteryless, and Wireless Capsule With Integrated Impedance and pH Sensors for Gastroesophageal Reflux Monitoring.* IEEE Transactions on Biomedical Engineering, 2012. **59**(11): p. 3131-3139.
63. Nishimura, T.H., et al. *A large air gap flat transformer for a transcutaneous energy transmission system*. in *Power Electronics Specialists Conference, PESC '94 Record., 25th Annual IEEE*. 1994.
64. Neagu, C.R., et al., *Characterization of a planar microcoil for implantable microsystems.* Sensors and Actuators A: Physical, 1997. **62**(1): p. 599-611.
65. Johannessen, E., et al., *Toward an injectable continuous osmotic glucose sensor.* Journal of Diabetes Science and Technology, 2010. **4**(4): p. 882-892.
66. Sodagar, A.M. and P. Amiri. *Capacitive coupling for power and data telemetry to implantable biomedical microsystems*. in *2009 4th International IEEE/EMBS Conference on Neural Engineering*. 2009.

67. Culurciello, E. and A.G. Andreou, *Capacitive Inter-Chip Data and Power Transfer for 3-D VLSI.* IEEE Transactions on Circuits and Systems II: Express Briefs, 2006. **53**(12): p. 1348-1352.
68. Asgarian, F. and A.M. Sodagar, *Wireless Telemetry for Implantable Biomedical Microsystems.* Biomedical Engineering, Trends in Electronics, InTech, 2011.
69. Romero, E., R.O. Warrington, and M.R. Neuman, *Energy scavenging sources for biomedical sensors.* Physiological Measurement, 2009. **30**(9): p. R35.
70. Schmidt, C.L. and E.R. Scott. *Energy harvesting and implantable medical devices - first order selection criteria*. in *2011 International Electron Devices Meeting*. 2011.
71. Beeby, S.P., M.J. Tudor, and N.M. White, *Energy harvesting vibration sources for microsystems applications.* Measurement Science and Technology, 2006. **17**(12): p. R175-R195.
72. Bullen, R.A., et al., *Biofuel cells and their development.* Biosensors and Bioelectronics, 2006. **21**: p. 2015-2045.
73. Andrea, C., et al., *Kinetic and thermal energy harvesters for implantable medical devices and biomedical autonomous sensors.* Measurement Science and Technology, 2014. **25**(1): p. 012003.
74. Settaluri, K.T., H. Lo, and R.J. Ram, *Thin Thermoelectric Generator System for Body Energy Harvesting.* Journal of Electronic Materials, 2012. **41**(6): p. 984-988.
75. Stark, I. and M. Stordeur. *New micro thermoelectric devices based on bismuth telluride-type thin solid films*. in *Thermoelectrics, 1999. Eighteenth International Conference on*. 1999.
76. Stark, I. *Invited Talk: Thermal Energy Harvesting with Thermo Life*. in *International Workshop on Wearable and Implantable Body Sensor Networks (BSN'06)*. 2006.
77. Halvorsen, E., *Energy harvesting from motion - Lecture notes - Micro sensors and actuators course*. 2008, Vestfold University College, Norway.
78. Goto, H., T. Sugiura, and T. Kazui. *Feasibility of the automatic generating system (AGS) for quartz watches as a leadless pacemaker power source: a preliminary report*. in *Proceedings of the 20th Annual International Conference of the IEEE Engineering in Medicine and Biology Society. Vol.20 Biomedical Engineering Towards the Year 2000 and Beyond (Cat. No.98CH36286)*. 1998.
79. Buren, T.v., et al., *Optimization of inertial micropower Generators for human walking motion.* IEEE SENSORS JOURNAL, 2006. **6**(1): p. 28-38.
80. Katic, J., *Highly-Efficient Energy Harvesting Interfaces for Implantable Biosensors*, in *KTH School of Information and Communication Technology*. 2017, KTH Royal Institute of Technology: Stockholm, Sweden.
81. Tashiro, R., et al., *Development of an electrostatic generator for a cardiac pacemaker that harnesses the ventricular wall motion.* Journal of Artificial Organs, 2002. **5**(4): p. 0239-0245.
82. Boisseau, S., G. Despesse, and B.A. Seddik, *Electrostatic Conversion for Vibration Energy Harvesting*, in *Small-Scale Energy Harvesting*. 2012: Intech.

83. Basaeri, H., D.B. Christensen, and S. Roundy, *A review of acoustic power transfer for bio-medical implants.* Smart Materials and Structures, 2016. **25**(12): p. 123001.
84. Kerzenmacher, S., *6 - Biofuel cells as sustainable power sources for implantable systems*, in *Implantable Sensor Systems for Medical Applications*, A. Inmann and D. Hodgins, Editors. 2013, Woodhead Publishing. p. 183-212.
85. Santiago, Ó., et al., *Review of implantable and external abiotically catalysed glucose fuel cells and the differences between their membranes and catalysts.* Applied Energy, 2016. **179**: p. 497-522.
86. Rao, J.R., et al., *The performance of glucose electrodes and the characteristics of different biofuel cell constructions.* Bioelectrochemistry and Bioenergetics, 1976. **3**(1): p. 139-150.
87. Basu, D. and S. Basu, *Performance studies of Pd–Pt and Pt–Pd–Au catalyst for electro-oxidation of glucose in direct glucose fuel cell.* International Journal of Hydrogen Energy, 2012. **37**(5): p. 4678-4684.
88. Kerzenmacher, S., et al., *A potentially implantable glucose fuel cell with Raney-platinum film electrodes for improved hydrolytic and oxidative stability.* Journal of Power Sources, 2011. **196**(3): p. 1264-1272.
89. Barton, S.C., J. Gallaway, and P. Atanassov, *Enzymatic Biofuel Cells for Implantable and Microscale Devices.* Chem. Rev. , 2004. **104**: p. 4867-4886

90. du Toit, H., et al., *Generating power from transdermal extracts using a multi-electrode miniature enzymatic fuel cell.* Biosensors and Bioelectronics, 2016. **78**: p. 411-417.
91. Tsujimura, S., *Glucose/O2 biofuel cell operating at physiological conditions.* Electrochemistry, 2002. **70**: p. 940.
92. Yahiro, A.T., S.M. Lee, and D.O. Kimble, *Bioelectrochemistry: I. Enzyme utilizing bio-fuel cell studies.* Biochimica et Biophysica Acta (BBA) - Specialized Section on Biophysical Subjects, 1964. **88**(2): p. 375-383.
93. Chen, T., et al., *A Miniature Biofuel Cell.* Journal of the American Chemical Society, 2001. **123**(35): p. 8630-8631.
94. Yu, E.H. and K. Scott, *Enzymatic Biofuel Cells—Fabrication of Enzyme Electrodes.* Energies 2010, 3, 23-42, 2010. **3**: p. 23-42.
95. Ayub, M., et al., *Precise electrochemical fabrication of sub-20 nm solid-state nanopores for single-molecule biosensing.* Journal of Physics-Condensed Matter, 2010. **22**(45).
96. Ivanov, I., T. Vidakovic-Koch, and K. Sundmacher, *Recent Advances in Enzymatic Fuel Cells: Experiments and Modeling.* Energies, 2010. **3**(4): p. 803-846.
97. Mano, N., F. Mao, and A. Heller, *Characteristics of a Miniature Compartment-less Glucose−O2 Biofuel Cell and Its Operation in a Living Plant.* Journal of the American Chemical Society, 2003. **125**(21): p. 6588-6594.
98. Kim, H.-H., et al., *A Miniature Membrane-less Biofuel Cell Operating under Physiological Conditions at 0.5 V.* Journal of The Electrochemical Society, 2003. **150**(2): p. A209-A213.

99. Sato, F., et al., *Enzyme-based glucose fuel cell using Vitamin K3-immobilized polymer as an electron mediator.* Electrochemistry Communications, 2005. **7**(7): p. 643-647.

100. Cinquin, P., et al., *A Glucose BioFuel Cell Implanted in Rats.* Plos One, 2010. **5**(5).

101. Justin, G.A., et al. *An investigation of the ability of white blood cells to generate electricity in biofuel cells*. in *Proceedings of the IEEE 31st Annual Northeast Bioengineering Conference, 2005.* 2005.

102. Potter, M.C., *Electrical Effects Accompanying the Decomposition of Organic Compounds.* Proceedings of the Royal Society of London. Series B, Containing Papers of a Biological Character, 1912. **84**(571): p. 260-276.

103. Davis, J.B. and H.F. Yarbrough, *Preliminary Experiments on a Microbial Fuel Cell.* Science, 1962. **137**(3530): p. 615.

104. Siu, C.P.B. and C. Mu, *A Microfabricated PDMS Microbial Fuel Cell.* Microelectromechanical Systems, Journal of, 2008. **17**(6): p. 1329-1341.

105. Davis, F. and S.P.J. Higson, *Biofuel cells—Recent advances and applications.* Biosensors and Bioelectronics 22 (2007) 1224–1235, 2007. **22**: p. 1224 - 1235.

106. Han, Y., C. Yu, and H. Liu, *A microbial fuel cell as power supply for implantable medical devices.* Biosensors and Bioelectronics, 2010. **25**(9): p. 2156-2160.

107. Dong, K., et al., *Microbial fuel cell as power supply for implantable medical devices: A novel configuration design for simulating colonic environment.* Biosensors and Bioelectronics, 2013. **41**: p. 916-919.

108. Kerzenmacher, S., et al., *An abiotically catalyzed glucose fuel cell for powering medical implants: Reconstructed manufacturing protocol and analysis of performance.* Journal of Power Sources, 2008. **182**: p. 66-75.

109. Zhao, Y., et al., *High-power non-enzymatic glucose biofuel cells based on three-dimensional platinum nanoclusters immobilized on multiwalled carbon nanotubes.* Electrochimica Acta, 2014. **145**: p. 159-169.

110. Rapoport, B.I., J.T. Kedzierski, and R. Sarpeshkar, *A Glucose Fuel Cell for Implantable Brain–Machine Interfaces.* PLoS ONE, 2012. **7**(6): p. e38436.

111. Carreau, A., et al., *Why is the partial oxygen pressure of human tissues a crucial parameter? Small molecules and hypoxia.* Journal of Cellular and Molecular Medicine, 2011. **15**(6): p. 1239-1253.

112. Bockris, J.O.M., B.J. Piersma, and E. Gileadi, *Anodic oxidation of cellulose and lower carbohydrates.* Electrochimica Acta, 1964. **9**(10): p. 1329-1332.

113. Warner, H. and B.W. Robinson, *A glucose cell*, in *Digest of the 7th International Conference on Medical and Biological Engineering*. 1967: Stockholm, Sweden. p. 520.

114. Wolfson, S.K., et al., *The bioautofuel cell: A device for pacemaker power from direct energy conversion consuming autgenous fuel.* Trans. Ams. Soc. Artif. Intern. Organs, 1968. **14**: p. 198-203.

115. Drake, R.F., et al., *A tissue implantable fuel cell power supply.* Trans. Ams. Soc. Artif. Intern. Organs, 1970. **16**: p. 199-205.

116. Wolfson, S.K.J., et al., *A single electrolyte fuel cell utilizing permselective membranes.* ASAIO Journal, 1970. **16**(1): p. 193-198.
117. Malachesky, P., et al. *Parametric studies of the implantable fuel cell*. in *7th Intersociety Energy Conversion Engineering Conference Proceedings, American Chemical Society*. 1972. Washington D.C.
118. Weidlich, E., et al., *Animal Experiments with Biogalvanic and Biofuel Cells.* Biomaterials, Medical Devices, and Artificial Organs, 1976. **4**(3-4): p. 277-306.
119. Stetten, F.v., et al., *Biofuel cells as micro power generators for implantable devices.* Proceeding of Eurosensors 2006: p. 222-225.
120. Kerzenmacher, S., et al., *A surface mountable glucose fuel cell for medical implants.* The 14th International Conference on Solid-State Sensors, Actuators and Microsystems, 2007: p. 125-128.
121. Kloke, A., et al., *A single layer biofuel cell as potential coating for implantable low power devices.* Proceeding of Eurosensors, 2008: p. 1416-1419.
122. Oncescu, V. and D. Erickson, *High volumetric power density, non-enzymatic, glucose fuel cells.* Scientific Reports, 2013. **3**: p. 1226.
123. Slaughter, G. and J. Sunday, *A membraneless single compartment abiotic glucose fuel cell.* Journal of Power Sources, 2014. **261**: p. 332-336.
124. Stetten, F.v., et al., *A one-compartment, direct glucose fuel cell for powering long-term medical implants.* MEMS 2006, 2006.
125. Colton, C.K. and R.F. Drake, *Analysis of in vivo deoxygenation of human blood: A feasibilty study for an implantable biological fuel cell.* ASAIO Journal, 1969. **15**(1): p. 187-198.
126. Kloke, A., et al., *Porous Platinum Electrodes Fabricated by Cyclic Electrodeposition of PtCu Alloy: Application to Implantable Glucose Fuel Cells.* The Journal of Physical Chemistry C, 2012. **116**(37): p. 19689-19698.
127. Oncescu, V. and D. Erickson, *A microfabricated low cost enzyme-free glucose fuel cell for powering low-power implantable devices.* Journal of Power Sources, 2011. **196**(22): p. 9169-9175.
128. Rao, R. and G. Richter, *Implantable fuel cell*, U. Grant, Editor. 1975: US.
129. Wan, B.Y.C. and A.C.C. Tseung, *Some studies related to electricity generation from biological fuel cells and galvanic cells,in vitro and in vivo.* Medical and biological engineering, 1974. **12**(1): p. 14-28.
130. Kozawa, A., V.E. Zilionis, and R.J. Brodd, *Electrode Materials and Catalysts for Oxygen Reduction in Isotonic Saline Solution.* Journal of The Electrochemical Society, 1970. **117**(12): p. 1474-1478.
131. Kerzenmacher, S., et al., *Raney-platinum film electrodes for potentially implantable glucose fuel cells. Part 2: Glucose-tolerant oxygen reduction cathodes.* Journal of Power Sources, 2010. **195**(19): p. 6524-6531.
132. Kloke, A., et al., *Cyclic Electrodeposition of PtCu Alloy: Facile Fabrication of Highly Porous Platinum Electrodes.* Advanced Materials, 2012. **24**: p. 2916-2921.
133. Köhler, C., et al., *Fabrication of highly porous platinum electrodes for micro-scale applications by pulsed electrodeposition and dealloying.* Journal of Power Sources, 2013. **242**: p. 255-263.

134. Kerzenmacher, S., et al., *An efficient low-power DC-DC converter enables operation of a cardiac pacemaker by an integrated glucose fuel cell.* PowerMEMS, 2008: p. 189-192.
135. Appleby, A.J. and C. Van Drunen, *Anodic Oxidation of Carbohydrates and Related Compounds in Neutral Saline Solution.* Journal of The Electrochemical Society, 1971. **118**(1): p. 95-97.
136. Kerzenmacher, S., et al., *A Binder-less Glucose Fuel Cell with Improved Chemical Stability Intended as Power Supply for Medical Implants.* ECIFMBE, 2008. **22**: p. 2379-2383.
137. Kerzenmacher, S., et al., *Raney-platinum film electrodes for potentially implantable glucose fuel cells. Part 1: Nickel-free glucose oxidation anodes.* Journal of Power Sources, 2010. **195**(19): p. 6516-6523.
138. Wilkinson, D.P., et al., *Proton Exchange Membrane Fuel Cells - Material Properties and Performance*, ed. S. Lee. 2009: CRC Press.
139. Fujiwara, N., et al., *Nonenzymatic glucose fuel cells with an anion exchange membrane as an electrolyte.* Electrochemistry Communications, 2009. **11**(2): p. 390-392.
140. ; Available from: https://www.fuelcellstore.com/.
141. Rao, J.R., et al., *Biological fuel cells for implanted electronic devices.* Ber. Busenges. Phys. Chem., 1973. **77**: p. 787-790.
142. Kloke, A., et al., *Electrodeposited thin-layer electrodes for the use in potentially implantable glucose fuel cells.* Transducer, 2009: p. 537-540.
143. Huang, K.-T., P.-C. Kuo, and Y.-D. Yao, *Formation of Pt nanorods on nanoporous anodic aluminum oxides by controlled nucleation sites.* Thin Solid Films, 2009. **517**(11): p. 3243-3247.
144. Yoo, S.-H., L. Liu, and S. Park, *Nanoparticle films as a conducting layer for anodic aluminum oxide template-assisted nanorod synthesis.* Journal of Colloid and Interface Science, 2009. **339**(1): p. 183-186.
145. Rodriguez, J.F., T. Mebrahtu, and M.P. Soriaga, *Determination of the surface area of gold electrodes by iodine chemisorption.* Journal of Electroanalytical Chemistry and Interfacial Electrochemistry, 1987. **233**(1): p. 283-289.
146. Monzón-Hernández, D., D. Luna-Moreno, and D. Martínez-Escobar, *Fast response fiber optic hydrogen sensor based on palladium and gold nano-layers.* Sensors and Actuators B: Chemical, 2009. **136**(2): p. 562-566.
147. Bard, A.J. and L.R. Faulkner, *Electrochemical Methods: Fundamentals and Applications, 2nd Ed.* 2001, John Wiley & Sons, Inc.
148. Grdeń, M., et al., *Electrochemical behaviour of palladium electrode: Oxidation, electrodissolution and ionic adsorption.* Electrochimica Acta, 2008. **53**(26): p. 7583-7598.
149. Łosiewicz, B., L. Birry, and A. Lasia, *Effect of adsorbed carbon monoxide on the kinetics of hydrogen electrosorption into palladium.* Journal of Electroanalytical Chemistry, 2007. **611**(1–2): p. 26-34.
150. Gołek, F., et al., *AFM image artifacts.* Applied Surface Science, 2014. **304**: p. 11-19.

151. Shen, J., et al., *AFM tip-sample convolution effects for cylinder protrusions.* Applied Surface Science, 2017. **422**: p. 482-491.
152. Ngamchuea, K., et al., *Planar diffusion to macro disc electrodes—what electrode size is required for the Cottrell and Randles-Sevcik equations to apply quantitatively?* Journal of Solid State Electrochemistry, 2014. **18**(12): p. 3251-3257.
153. Abreu, J.B., et al., *Electrochemical digital etching in non-corrosive electrolyte: I(ads)-catalyzed dissolution and reordering of ion-bombarded Pd(111).* Journal of Electroanalytical Chemistry, 1995. **381**(1): p. 239-241.
154. Rand, D.A.J. and R. Woods, *The nature of adsorbed oxygen on rhodium, palladium and gold electrodes.* Journal of Electroanalytical Chemistry and Interfacial Electrochemistry, 1971. **31**(1): p. 29-38.
155. Piela, B. and P.K. Wrona, *Capacitance of the gold electrode in 0.5 M H2SO4 solution: a.c. impedance studies.* Journal of Electroanalytical Chemistry, 1995. **388**(1–2): p. 69-79.
156. Fang, L.-l., et al., *Determination of the Real Surface Area of Palladium Electrode.* Chinese Journal of Chemical Physics, 2010. **23**(5): p. 543.
157. Buividas, R., et al., *Novel method to determine the actual surface area of a laser-nanotextured sensor.* Applied Physics A, 2013. **114**(1): p. 169-175.
158. Czerwiński, A., *The adsorption of carbon oxides on a palladium electrode from acidic solution.* Journal of Electroanalytical Chemistry, 1994. **379**(1): p. 487-493.
159. Woods, R., *Chemisorption at Electrodes: Hydrogen and Oxygen on Noble Metals and their Alloys*, in *Electroanalytical chemistry: a series of advances*, A.J. Bard, Editor. 1976, Dekker: New York. p. 1-162.
160. Srinivasan, S., *Fuel Cells - From Fundamentals to Applications*. 2006: Springer US.

Collection of Publications

Article 1

J Mater Sci

Title: Thin film nanoporous electrodes for the selective catalysis of oxygen in abiotically catalysed micro glucose fuel cells

Authors: Uyen P. Do, Frode Seland, Michel M. Maharbiz, Kaying Wang, Oivind Johannesen, Erik A. Johannessen

Journal: Journal of Materials Science

Volume: 51, **Issue:** 19, **Pages:** 9095-9107

Date of Publication: 06 July 2016

DOI: 10.1007/s10853-016-0162-7

Articles omitted from online publication due to publisher's restrictions

Article 2

Title: The Real Area of Nanoporous Catalytic Surfaces of Gold and Palladium in Aqueous Solutions

Authors: Uyen P. Do, Frode Seland, Erik A. Johannessen

Journal: Journal of the Electrochemical Society

Volume: 165, **Issue:** 5, **Pages:** H219-H228

Date of Publication: 24 March 2018

DOI: 10.1149/2.0341805jes

Articles omitted from online publication due to publisher's restrictions

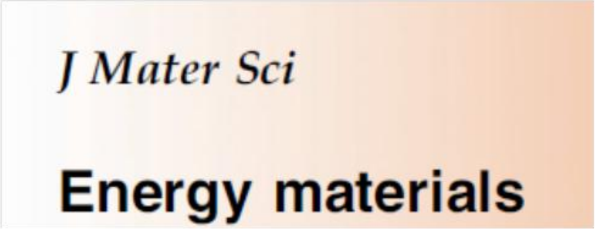

J Mater Sci

Energy materials

Article 3

Title: Raney-platinum thin film electrodes for the catalysis of glucose in abiotically catalyzed micro-glucose fuel cells

Authors: Uyen P. Do, Frode Seland, Kaying Wang, Erik A. Johannessen

Journal: Journal of Materials Science

Volume: 54, **Issue:** 22, **Pages:** 14143-14156

Date of Publication: 13 August 2019

DOI: 10.1007/s10853-019-03907-9

Articles omitted from online publication due to publisher's restrictions

Article 4

Title: A micro fuel cell for abiotical catalysis of glucose

Authors: Uyen P. Do, Frode Seland, Erik A. Johannessen

Journal: Journal of Power Sources

Volume: 478, Page: 229032

Date of Publication: 12 October 2020

DOI: https://doi.org/10.1016/j.jpowsour.2020.229032

Articles omitted from online publication due to publisher's restrictions

Doctoral dissertation no. 88
2021

—

Glucose energy harvester for self-powering of remote distributed bioanalytical microsystems
Dissertation for the degree of PhD

—

Uyen Phuong Do

—

ISBN: 978-82-7860-465-6 (print)
ISBN: 978-82-7860-464-9 (online)

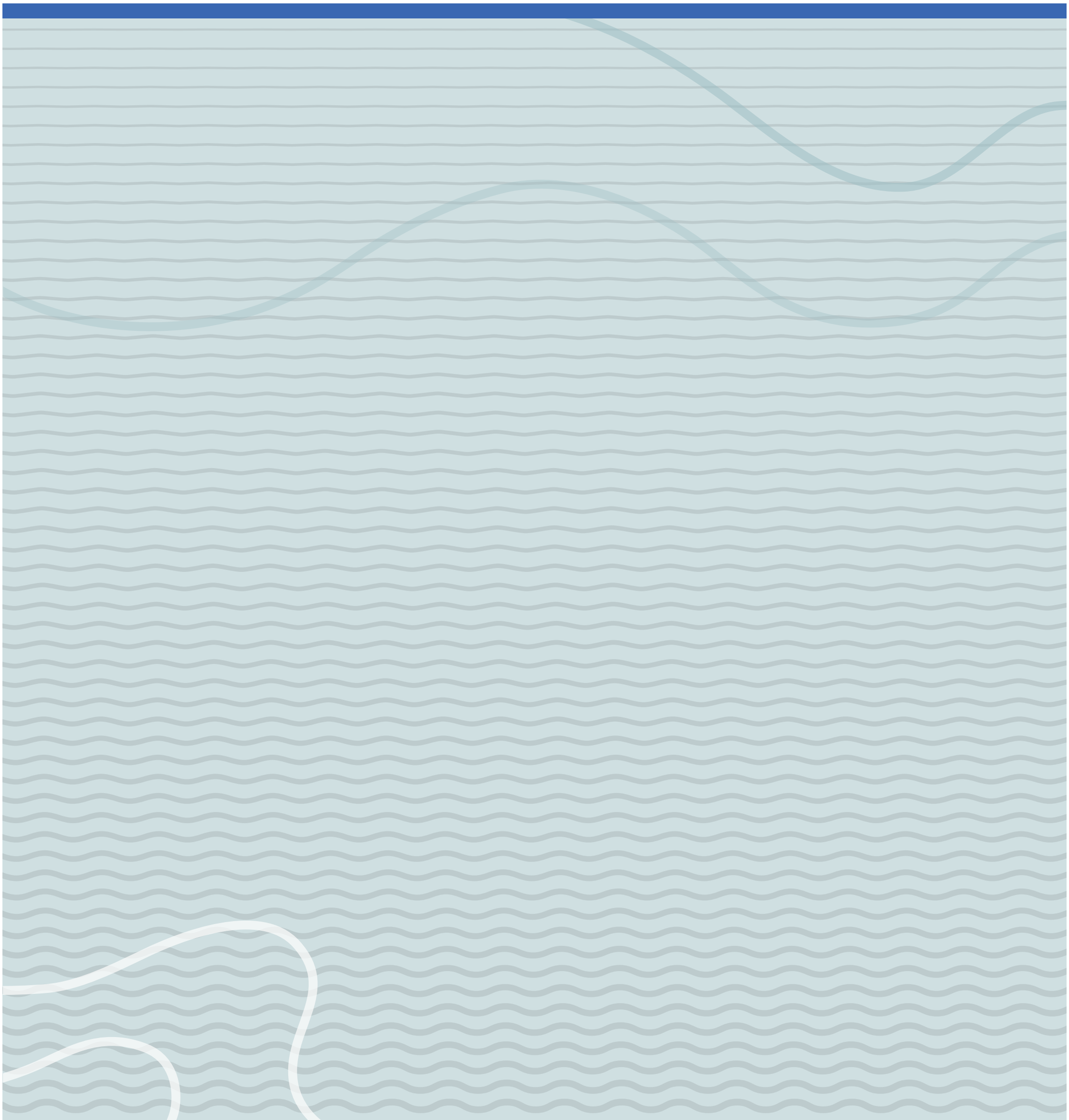usn.no